

RUBBLE CHARACTERISTICS ASSOCIATED WITH ROOM COLLAPSE AT THE WASTE ISOLATION PILOT PLANT: IMPACT OF SALT CLAST SHAPES AND SIZE DISTRIBUTIONS ON THE DEPOSITIONAL PORE SYSTEM

Robert Lander¹, Edward Matteo², Linda Bonnell¹, Thomas Dewers², Melisa Mills², James Guilkey³, Chven Mitchell², John Stormont⁴

¹Geocosm LLC, Durango, CO, USA; ²Sandia National Laboratory, Albuquerque, NM, USA; ³University of Utah, Department of Mechanical Engineering, Salt Lake City, UT, USA; ⁴University of New Mexico, Albuquerque, NM, USA

Correspondence to:

Robert Lander, roblander@ geocosm.net Geocosm, 10 Town Plaza #233, Durango, CO 81301, USA

How to Cite:

Lander, R., Matteo, E., Bonnell, L., Dewers, T., Mills, M., Guilkey, J., Mitchell, C., & Stormont, J. (2025). Rubble Characteristics Associated with Room Collapse at the Waste Isolation Pilot Plant: Impact of Salt Clast Shapes and Size Distributions on the Depositional Pore System. InterPore Journal, 2(3), IPJ250825-3. https://doi.org/10.69631/

RECEIVED: 23 Sept. 2024 ACCEPTED: 1 July 2025 PUBLISHED: 25 Aug. 2025

ipj.v2i3nr45

ABSTRACT

The fluid transport properties of rubble associated with disposal room collapse within layered salt deposits at the Waste Isolation Pilot Plant (WIPP) in southeastern New Mexico, USA are of concern when evaluating repository performance. Although properties of crushed salt have been studied extensively, salt rubble characteristics are less well known, while also being more difficult to characterize and model given the broader associated range in clast sizes. We describe a methodology for assessing rubble porosity and three-dimensional internal structure through deposition simulations that use high-fidelity renditions of clast shapes and that consider a broad range in clast sizes. We demonstrate the application of this approach using clast size and shape data that we collected on run of mine (ROM) material from WIPP, which represents the best available proxy for rubble material. Clast sizes from sieve analysis span ~1–100 mm with a mass weighted mean value of 13 mm. Simulated rubble deposits have interclast porosity values ranging from 34.1-38.6 vol% (n = 6). The largest clasts in these simulations tend to be underlain by the largest pores. Thus, although these clasts act as barriers for flow, they also are associated with highly permeable but localized flow paths. Scenarios involving alternative input configurations reveal that porosity values are highly sensitive to clast size variability (~10 vol% greater for nearly uniform compared to highly variable clast size distributions), clast shape (~10-13 vol% greater when using ROM shapes compared to spheres), and the extent of induced rearrangement (~3 vol% lower with limited rearrangement and ~10 vol% lower for extensive rearrangement). Porosity also is strongly affected by frictional coefficient values (~10 vol% lower for μ = 0.05 compared to μ = 1.0), but less so for values within the range of uncertainty for salt clasts (2 vol% lower for $\mu = 0.62$ compared to

Lander, et al. Page 2 of 28

KEYWORDS

Nuclear waste storage, Nuclear waste disposal, Waste isolation pilot plant, Granular media, Porosity, Grain shape, Polydispersity



This is an open access article published by InterPore under the terms of the Creative Commons Attribution-NonCommercial-NoDerivatives 4.0 International License (CC BY-NC-ND 4.0) (https://creativecommons.org/licenses/by-nc-nd/4.0/).

1. INTRODUCTION

An essential consideration when gauging the potential magnitude of radionuclide release from nuclear waste sites is the fluid storage and transport properties of the repository. Although models have been developed for simulating the porosity and permeability for rooms with waste containers and crushed salt backfill (10, 54), none exist for rubble deposits that form in response to the collapse of empty or incompletely filled rooms in disposal sites that are located in salt deposits. In this contribution we describe a methodology for simulating the properties of such rubble deposits.

Room collapse is a concern at the Waste Isolation Pilot Plant (WIPP) situated in southeastern New Mexico, USA (**Fig. 1**). Several rooms and access drifts at WIPP were abandoned following the release of radiation in 2014 (65, 66). As illustrated in **Figure 2**, rubble deposits are likely to form in such areas. Accurately simulating the porosity and permeability of salt rubble deposits associated with room collapse at WIPP is a difficult challenge given that the associated clasts display a large range in size while also having complex and heterogeneous shapes. (*To avoid confusion, we use the term "clast" when describing the discrete solid objects that comprise rubble deposits given that the term "grain" often is used to refer to crystal domain size in the salt literature.)*

The WIPP serves as an active geological repository for the storage of transuranic nuclear waste and lies within a ~600 m thick deposit of salt within the Permian Salado Formation of the Delaware Basin (46). Waste containers are stored in rooms cut into this layered salt deposit that are ~660 meters below the surface (Fig. 1; 47). Under undisturbed conditions, the rate at which radionuclides are released into the biosphere is expected to be negligible (65). If the WIPP were to be penetrated by a borehole, however,

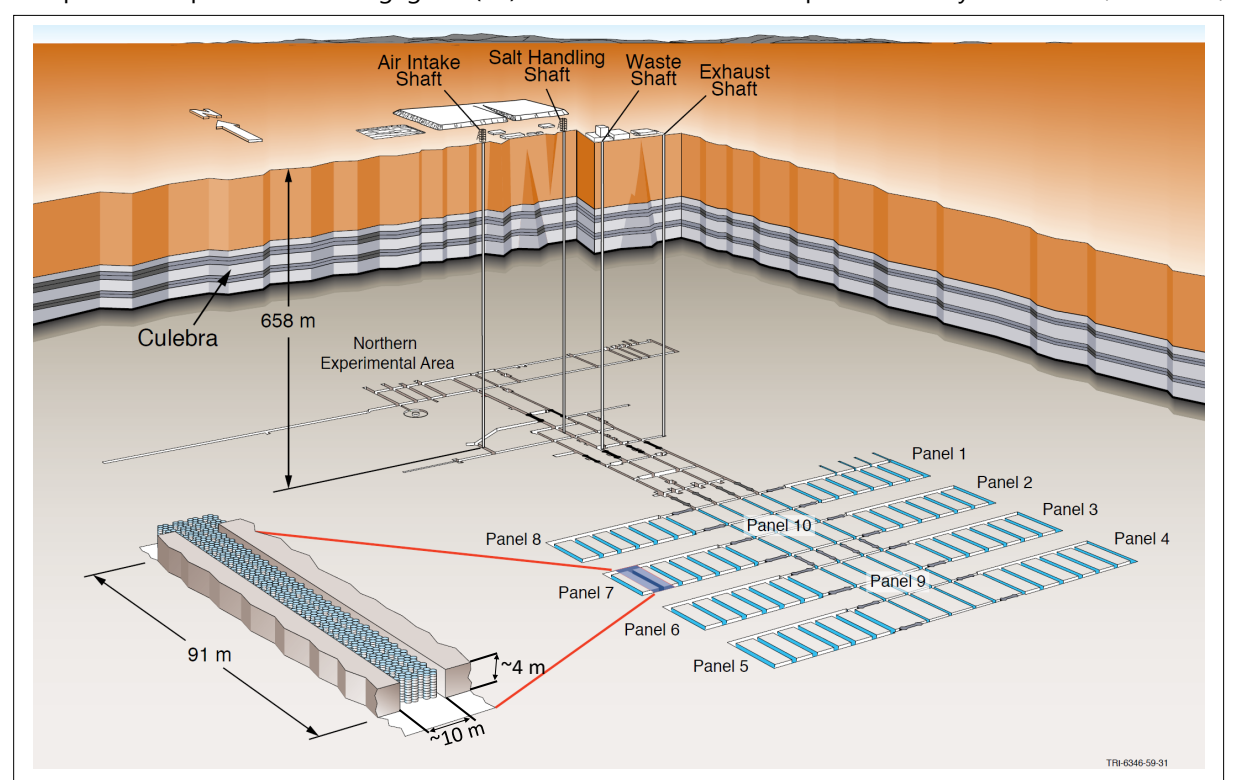


Figure 1: Layout of WIPP site (from 47). Republished with the permission of Sandia National Laboratories.

Lander, et al. Page 3 of 28

this could potentially result in the flooding of the repository by brine, enabling the transport of radionuclides into highly permeable dolostones within the overlying Culebra layer (**Fig. 1**; 47). Moreover, chemical reactions occurring within the repository in response to brine incursion could generate gases that increase the risk of radionuclide release through boreholes (47). The porosity and permeability of the repository will be important factors affecting the extent of radionuclide release in such scenarios.

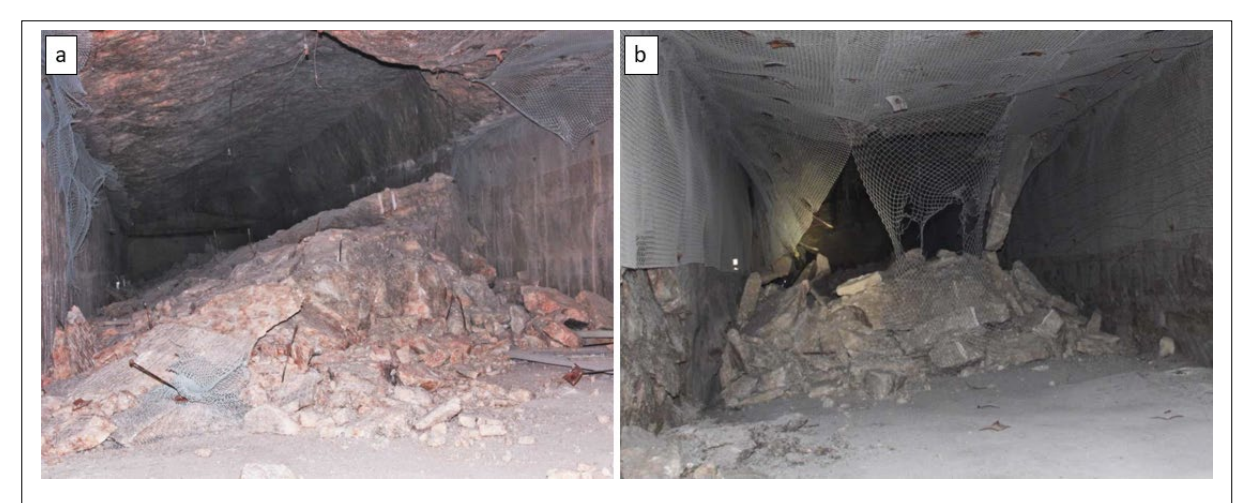


Figure 2: Salt rubble within partially collapsed WIPP rooms (R. Carrasco personal communication, September 2019; 47). **(a)** Room 4, Panel 7, November 2016. The room is ~10m wide. **(b)** E300-S3650 access drift, September 2016. *Republished with the permission of Sandia National Laboratories*.

The geomechanical and fluid transport properties of granular crushed salt have been studied in detail given its importance as a packing material for backfilled rooms in nuclear waste disposal sites (4, 7, 8, 9, 11, 21, 22, 23, 26, 28, 49, 50, 51, 56, 57, 63). By contrast, the properties of salt rubble deposits associated with chamber collapse are less well known, although they have been the subject of recent investigations by Mills et al. (38), Reedlunn et al. (47), Matteo et al. (36), and Babcock (3). Compared to crushed salt, rubble deposits have a far greater variation in the sizes and shapes of associated clasts. Studies of the deposition, internal structure, and bulk properties of granular media indicate that deposit characteristics are highly sensitive both to clast size distributions and shapes (2, 5, 6, 12, 14, 19, 20, 25, 27, 33, 34, 40, 43, 44, 58, 61, 67, 68). Most previous investigations of the properties of granular media, however, consider far simpler shapes compared to rubble clasts from the WIPP site while evaluating narrower ranges in clast sizes. The simulation methodology that we describe in this contribution attempts to address the challenges posed by the sizes and shapes of rubble clasts. A primary objective of this effort is the development of an approach that is capable of accurately predicting rubble porosity and internal structure given the importance of these characteristics for geomechanical and fluid transport properties.

As part of our analysis, we characterized properties of run of mine (ROM) material from the WIPP site, which represents the best available proxy for rubble resulting from room collapse. We used sieve analysis to determine the clast size distribution and high-resolution X-ray microtomography (micro-CT) imaging to obtain representative clast shapes. These data represent input constraints for a set of simulations of rubble depositional porosity and internal structure. Our simulation methodology employs a recently developed approach that can incorporate high-resolution depictions of clast shapes and a broad range in clast sizes. This method has been used to accurately reproduce sandstone microstructural characteristics, geomechanical properties, and permeabilities (32). Here we also evaluate simulation performance by comparing the result of deposition simulations of monodisperse (uniform size) spheres with laboratory experiments. Additionally, we show that a simulation involving WIPP ROM clast size distributions and shapes can reproduce the observed angles of repose of this material while using realistic frictional properties.

The simulations described here provide an assessment of rubble deposit porosity and internal structure given WIPP ROM characteristics. Additionally, we explore the sensitivity of the simulated porosity and

Lander, et al. Page 4 of 28

internal structure to several factors that may influence rubble properties, including the effects of induced clast rearrangement, uncertainties in frictional properties, and variations in clast shapes and size distributions. The packs that result from this effort also serve as input for simulation of permeability using computational fluid dynamics methods (the focus of ongoing investigations) as well as for simulation of consolidation in response to room collapse (19, 30).

2. MATERIALS AND METHODS

At the WIPP site, the Permian Salado Formation is made up of nearly pure halite, with <5 wt% mineral impurities, although some intervals incorporate polyhalite, anhydrite, dolomite, or clay (46, 52, 55). Rooms at WIPP are ~4 m high, ~10 m wide, and ~90 m long, and are arranged in arrays where rooms are separated by 36 m (Fig. 1). Roof collapse in such rooms often initiates at thin clay-rich intervals above the room ceilings (47). The clasts associated with roof collapse vary in size from less than 1 mm to well over 1 m (Fig. 2).

Due to safety concerns, it is not possible to sample rubble material from collapsing rooms at the WIPP site. The best available proxy for rubble deposits is the material produced by the mining machine that is used to excavate the repository. Consequently, in this study we used run of mine material that was collected from the floor of a room at the WIPP site for characterization of clast shapes and the clast size distribution (36).

2.1. Sieve analysis and clast shape characterization

We determined the clast size distribution for the run of mine sample by sieve analysis, focusing on clasts that could pass through a sieve opening of 76.2 mm. The "min" column in **Table 1** represents the opening size for the associated sieve whereas the "max" value indicates the opening size of the sieve that material passed through to reach this sieve. Consequently, the Mass Fraction for a table row represents the normalized mass fraction of clasts that are capable of passing through the max opening size but not the min opening size. The plot of sieve mass fraction with size uses the mid-point between the min and max values (**Fig. 3**). Material <1 mm in size is combined into the finest fraction in this plot given low associated abundances.

We used micro-CT imaging^a to compile a library of shapes for clasts from each sieve fraction in **Table 1** with a min opening size >1 mm. To ensure that the micro-CT images were of individual clasts and not aggregates, we placed representative clasts from each sieved fraction on a flat surface such that they were not in contact prior to imaging. Digital radiography acquisition^b and CT reconstruction and visualization^c software were used for image acquisition and reconstruction, respectively. Data processing included the application of a variety of filters to improve contrast in image intensity between solids and air, including a median filter and edge-preserving smoothing. The processed image data were then subjected to threshold segmentation techniques

Table 1: Clast size distribution as determined by sieve analysis for a run of mine (ROM) sample from the Waste Isolation Pilot Plant.

Sieve	Opening	Mass			
	Min Max		Fraction		
Α	38.100	76.200	0.081		
В	B 19.050 C 9.525		0.112 0.181		
С					
#4	4.750	9.525	0.283		
#6	3.353	4.750	0.122		
#8	2.380	3.353	0.104		
#10	1.999	2.380	0.044		
#12	1.679	1.999	0.030		
#14	1.410	1.679	0.016 0.007		
#16	1.191	1.410			
#18	1.001	1.191	0.004		
#20	0.841	1.001	0.003		
#25	0.706	0.841	0.002		
#30	0.594	0.706	0.001		
#40	0.419	0.594	0.002		
#50	0.297	0.419	0.001		
#60	0.249	0.297	0.001		
#80	0.178	0.249	0.001		
#100	0.150	0.178	0.000		
#200	0.074	0.150	0.002		
Pan		0.074	0.002		

^a North Star Imaging X50 micro-CT scanner (https://4nsi.com/) +Perkin Elmer 0822 1622 digital image detector (https://www.perkinelmer.com/)

b North Star efX-DR Software: https://4nsi.com/product/efx-dr-software/

c North Star efX-CT software: https://4nsi.com/product/efx-ct-software/

Lander, et al. Page 5 of 28

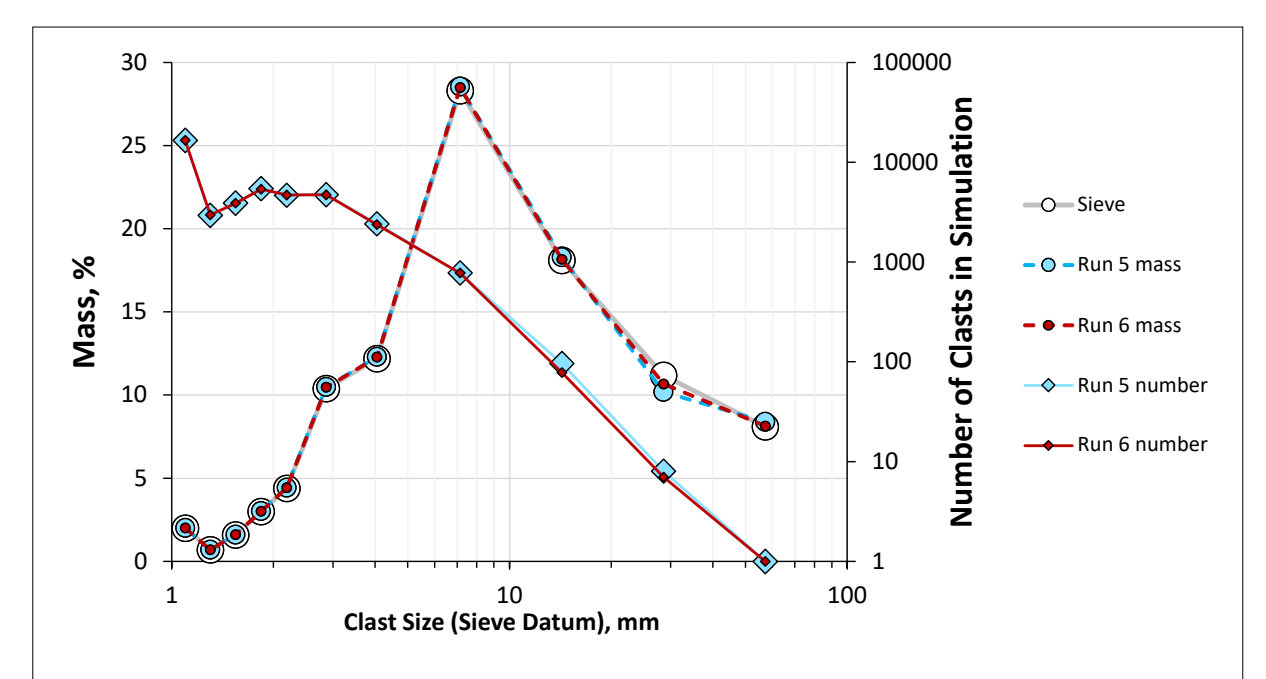


Figure 3: Circle symbols indicate mass fraction as determined by sieve analysis of ROM material (**Table 1**) and as used in runs 5 and 6 (**Table 2**). Diamond symbols show the number of clasts in each size bin for the run 5 and 6 deposition realizations. The mass and number of clasts <1 mm in size are included in the 1 mm point.

to isolate individual salt clasts. We used 3D image processing software^d to create closed "watertight" triangular surface meshes of the clast shapes based on voxel representations.

Collectively, we obtained 176 clast shapes from eleven size fractions, corresponding to sieves with minimum opening sizes ranging from 1 mm to 38.1 mm, as listed in **Table 1** (e.g., **Fig. 4**, **Fig. 5**, **Fig. 6**, and **Fig. 7**). The voxel resolution for clasts from sieve fractions with openings greater than 9.5 mm is 182 microns, for Sieve #4 (4.8-9.5 mm) is 83.5 microns, and for all remaining clasts is 38.1 microns (<4.8 mm; Sieves #6-#18).

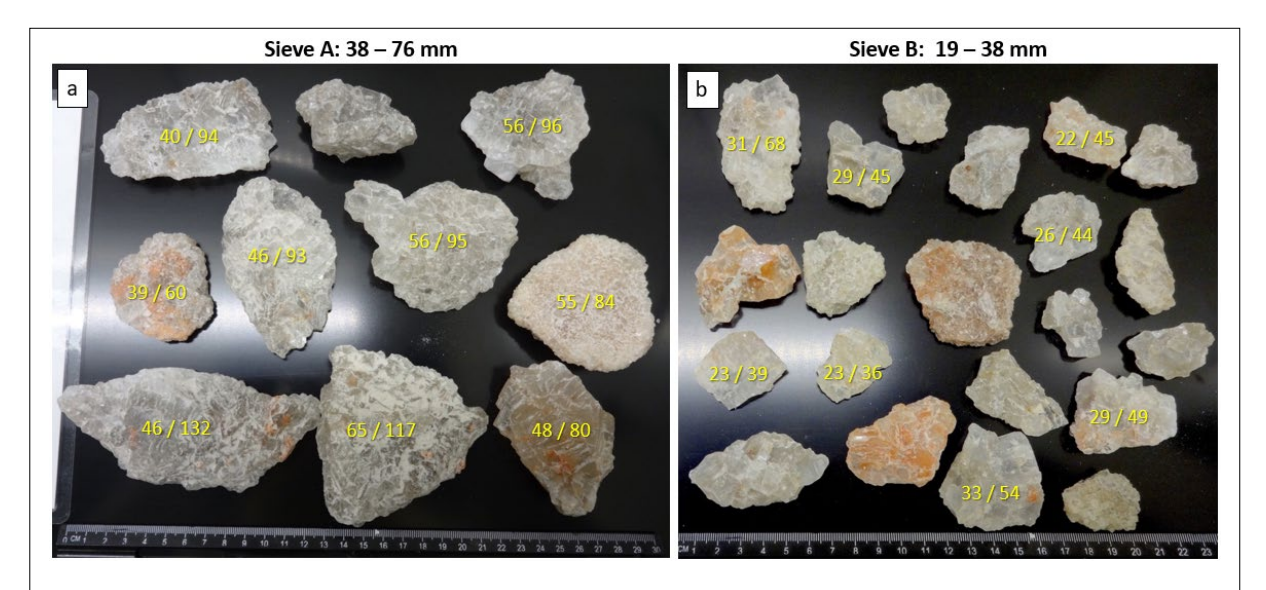


Figure 4: Example shapes of clasts obtained from **(a)** Sieve A (38-76 mm) and **(b)** Sieve B (19 to 38 mm) separates. The numbers on the left side of the clasts represent the estimated minimum sieve opening that they could pass through whereas the right value shows the long-axis length. Values are in mm.

d Simpleware™ software: https://www.synopsys.com/simpleware.html

Lander, et al. Page 6 of 28

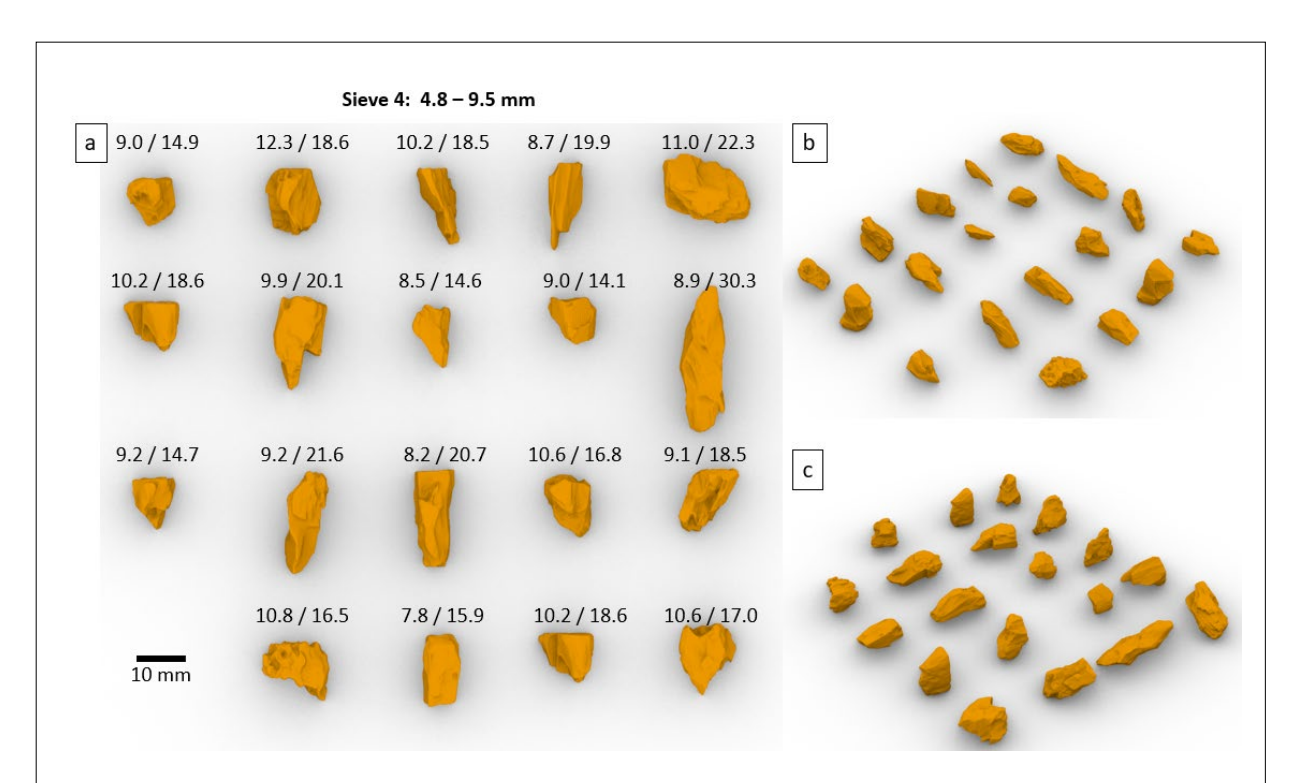


Figure 5: Geometries from micro-CT scans of clasts from Sieve 4 separates (4.8 - 9.5 mm). (a) The first number indicates the estimated minimum sieve pass through size and the second number shows the long axis. Values are in mm. (b) & (c) Alternative perspectives of the clasts.

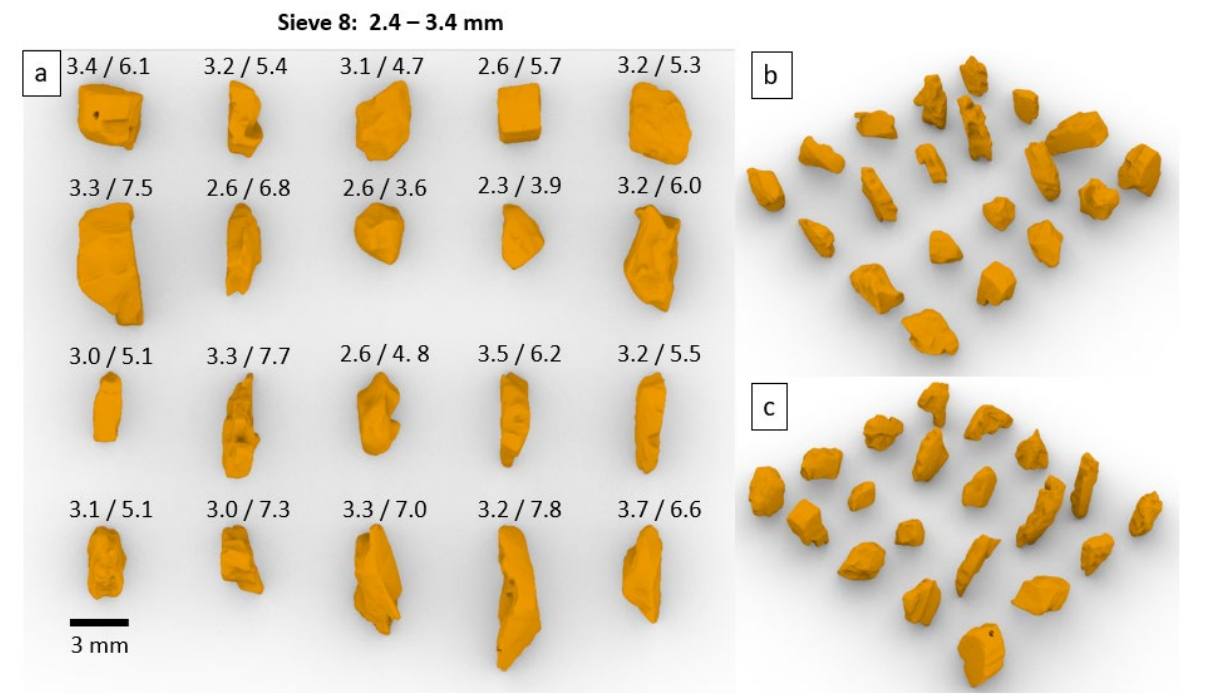


Figure 6: Geometries from micro-CT scans of clasts from Sieve 8 separates $(2.4 - 3.4 \, \text{mm})$. **(a)** The first number indicates the estimated minimum sieve pass through size and the second number shows the long axis. Values are in mm. **(b)** & **(c)** Alternative perspectives of the clasts.

Lander, et al. Page 7 of 28

One objective of the simulation approach is to ensure that size-dependent variations in clast shapes are honored. Therefore, shapes from micro-CT analysis are cataloged in a shape library according to the associated size bin from the sieve analysis. In this way simulated clasts are assigned shapes from appropriately sized library entries.

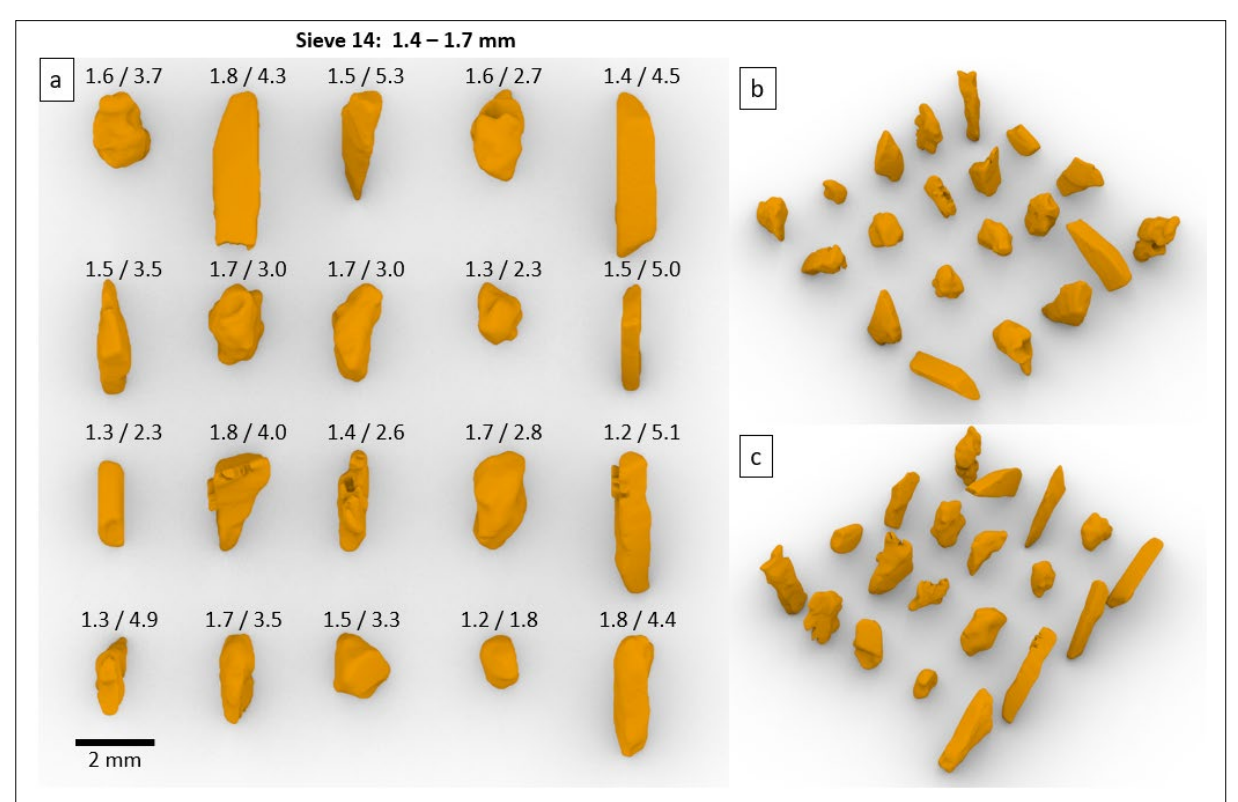


Figure 7: Geometries from micro-CT scans of clasts from Sieve 14 separates (1.4 – 1.7 mm). (a) The first number indicates the estimated minimum sieve pass through size and the second number shows the long axis. Values are in mm. (b) & (c) Alternative perspectives of the clasts.

2.2. Deposition simulations

We used Geocosm's Cyberclastic[™] software^e to simulate how falling clasts collide and rearrange as they are deposited as rubble (35). This simulator uses the PhysX® rigid body physics engine (v. 4.1 and v. 5.1; 41, 42) for clast movement, collision detection, and contact resolution. Each particle collision satisfies the laws for angular and linear momentum. Collisions are detected through a broad-phase and narrow-phase analysis procedure (41, 42), applied to aggregates of convex mesh hulls that represent clasts, the deposition container, and, where applicable, a piston is used to induce clast rearrangement. An iterative rigid body solver that is optimized for parallel processing is used to maximize computational throughput while minimizing contact jitter (62). A limitation of the current implementation is that breakage or deformation associated with clast collisions is not considered.

A factor that led us to apply this deposition simulation approach is its ability to work with high-resolution triangular surface meshes that can represent clasts with highly irregular shapes. This capability not only leads to high fidelity in the simulation of clast deposition, but also is designed to provide the input geometry used for Cyberstone™ simulations of compaction and geochemical reactions on sediment and rock microstructure, and the resulting impact on fluid transport and geomechanical properties (e.g., 18, 32). The results of this study, for example, are used as a starting point for Cyberstone simulations of compaction with various constitutive models and stress/strain boundary conditions (19, 30).

e https://geocosm.net

Lander, et al. Page 8 of 28

Input data for deposition simulations include:

• The **volume abundance of each clast type**, although simulations in this study assume that all clasts are made up of halite.

- The **volume-weighted size distribution for each clast type** where size in this study is defined as the smallest sieve opening dimension a clast can pass through.
- The **density, coefficient of restitution** (the ratio of the relative velocity of separation of two objects after a collision to the relative velocity of approach before the collision), and **dynamic and static frictional coefficients for each clast**. Unless stated otherwise, and consistent with halite composition, simulations assume values of 2.16 g/cm³, 0.22 (59), 0.77, and 0.77, respectively, for these properties across all clasts.
- Three-dimensional (3D) shape libraries. In this study 176 representative clasts from WIPP ROM are linked to 11 sieve size fractions, as described in section 2.1. Additionally, some simulations involve the use of spheres as discussed in sections 3.2.1 and 3.3.4.

This input data is used to make a deposition schedule for the simulation (31, 32). The first step in creating the schedule is to determine the volume of deposited material. This is done by specifying the interior diameter of a cylindrical container and estimating both the final deposit height and the depositional porosity. These estimates do not dictate the final result but do provide a basis for determining the solid volume of material that will be considered in the simulation. The next step in the process involves creating the individual clasts that will be deposited. This step includes determining the solid volume for each clast type, although in this study only halite clasts were considered. For each clast type the next step is to determine the absolute volume that will be deposited for each size increment in the associated size distribution. In the case of simulations that use the ROM size distribution, these size increments reflect the sieve results illustrated in Figure 3. For each of the size distribution bins, the system randomly selects a mesh from appropriately sized entries in the shape library, and scales it to a randomly determined size within the range of the bin. The volume for this mesh is subtracted from the volume yet to be assigned to the deposition schedule for the size bin. This clast creation process continues until the target volumes for each bin size of each clast type have been represented in the deposition schedule. In simulations for this study, the order of the clasts in the schedule is then randomized. Different random number seeds are used to create alternative, but statistically equivalent, deposition schedule realizations.

The end result of a depositional simulation is a 3D pack of clasts within a vertically oriented cylindrical container. Packs are trimmed into smaller cuboid forms to avoid packing artifacts near the container boundaries and to provide convenient boundary conditions for compaction and pore-scale fluid-flow simulations in subsequent studies.

2.2.1. Clast collision boundaries

Accurately detecting collisions among clasts is a crucial aspect of simulating deposition, but is computationally challenging for objects with concave regions such as those associated with the pits and cavities on salt clast surfaces (e.g. Fig. 8). Fortunately, collision detection for objects with convex surfaces is much simpler. We employed the hierarchical approximate convex decomposition approach introduced by Mamou (35) to represent clast shapes. This method enabled us to represent each individual clast as a connected set of convex surface meshes that result in an aggregate geometry that reproduces the overall clast shape, including pits and cavities. As an example, the clast depicted in Figure 8 is represented by 97 convex hulls, each of which is defined by a triangular surface mesh with 32 vertices. Although these hulls do not exactly replicate the original triangular surface mesh of the clast, they provide a close approximation that yields accurate impact and packing geometries. When generating the final depositional geometry for the rubble deposits, we replaced the approximation used in the rigid-body physics simulation with the original triangular surface mesh of the clast shape. In the example in Figure 8, this mesh was characterized using ~500,000 vertices. Using the source clast geometry ensures that the full complexity of the clast shape is preserved for downstream simulations that use deposition

Lander, et al. Page 9 of 28

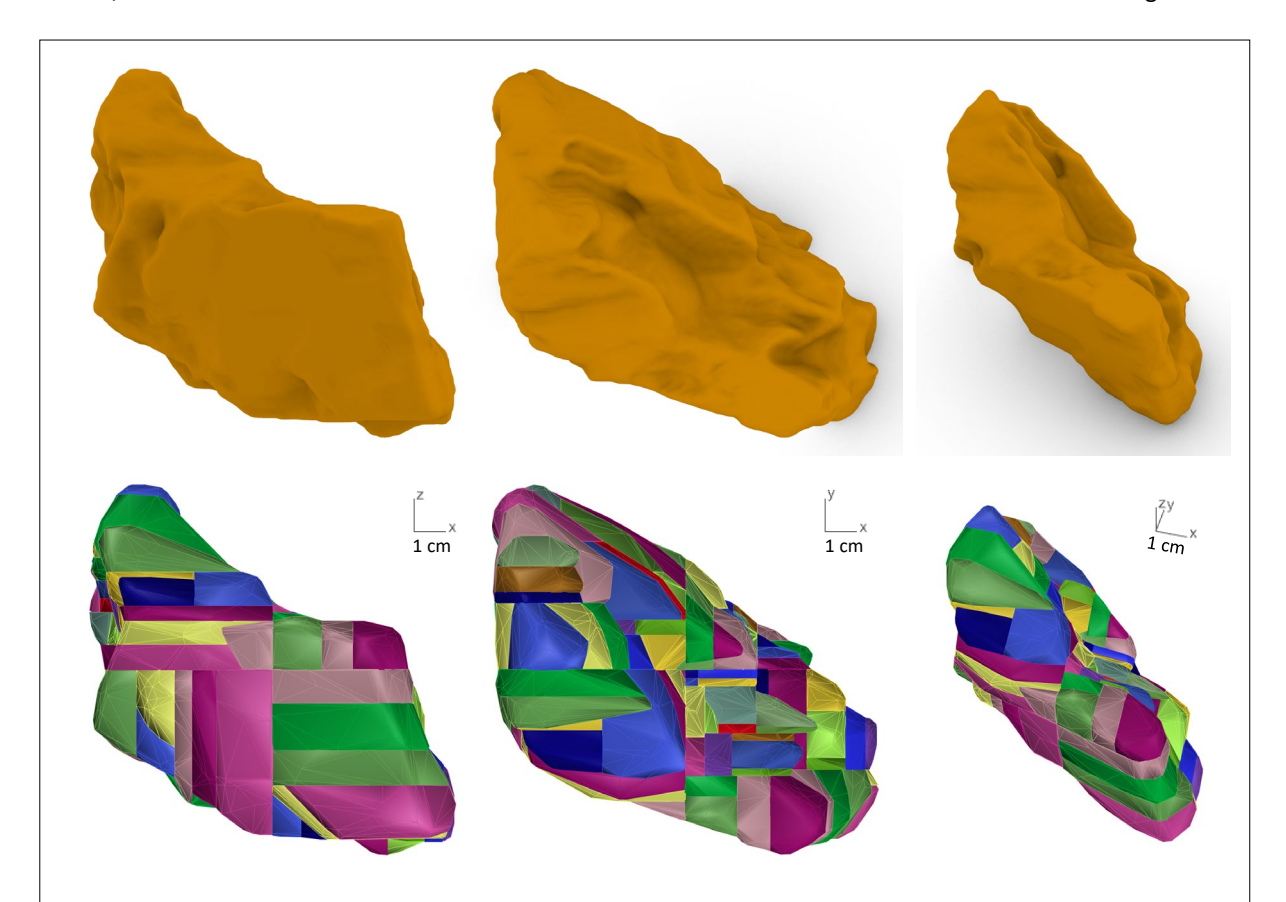


Figure 8: Three perspectives of a salt rubble clast with a long axis of 18.5 mm. The top row of images shows the triangular surface mesh that is derived from a micro-CT scan whereas the bottom row of images shows the 97 convex hulls that approximate the clast shape for collision detection in deposition simulations.

results as input, such as those involving pore-scale flow simulations to derive permeability or the analysis of rubble consolidation under loading. The replacement of the lower resolution collision boundary meshes with high-resolution shapes did not result in significant overlap among the clasts within the deposition simulations.

2.2.2. Clast shapes

As mentioned in section 2.2, when clasts are created, their shapes are derived from appropriate entries in the shape library. For simulations involving micro-CT segmented shapes from WIPP ROM material, when a clast is created for the deposition schedule, the associated shape is selected randomly from the micro-CT library entries for the sieve size bin with the closest clast size as measured in Krumbein (29) phi scale (Eq. 1) where D is the clast size in mm.

$$\varphi = -\log_2(D) \tag{1}$$

Thus, these deposition simulations preserve the size-dependent variations in shape that are represented in the library. Such simulations have "Micro-CT" entries under the "Clast Shape" column in **Table 2**.

The simulations with "Sphere" in the "Clast Shape" column of **Table 2** used spherical shapes with collision hulls that were represented by 512 vertices. Deposition simulations involving spheres were used for three purposes in this study. The first of these was to evaluate the accuracy of the deposition simulation approach by comparing results with well constrained laboratory measurements involving spheres (section 3.2.1). In this case, deposition and rearrangement simulations used a uniform (monodisperse) sphere size. The second purpose was to demonstrate that simulations involving spheres are unable to reproduce observed angles of repose of WIPP ROM rubble piles, unlike those that use ROM micro-CT derived shapes (section 3.2.2). The final objective for simulations involving spheres was to gauge the impact of clast shape on pack porosity and internal structure by comparing polydisperse simulations

Lander, et al. Page 10 of 28

made using spheres with otherwise equivalent simulations that use shapes from WIPP ROM material (section 3.3.4).

2.2.3. Clast size distributions

Many simulations in this study used size bins and volume fractions that were based on the sieve analysis of the WIPP ROM sample (**Table 1**), except that the volumes for all clasts from the <1.19 mm sieve separates were combined such that they fall in the 1.0 to 1.19 mm size bin (Sieve #18) as illustrated in **Figure 3**. Such simulations have "WIPP ROM Sieve" entries for the "Size Distribution" column in **Table 2**. In addition to using the clast size distribution from sieve analysis of the WIPP ROM samples, we included a series of simulations where we used ROM shapes, but varied the clast size distribution. These simulations employed log-normal size distributions representing various polydispersity values and were denoted by "Log normal" entered in **Table 2**. "Uniform" entries in the "Size Distribution" column indicate simulations involving monodisperse spheres, as described in sections 2.2.2 and 3.2.1.

Table 2: Simulation configurations and associated interclast porosity values. "N.A." indicates not applicable and "WIPP ROM Sieve" indicates sieve-derived size measurements made on run of mine material from the Waste Isolation Pilot Plant.

ĸun	number & name	Run type	Deposition	Clast	SD	Size	Friction	Porosity	Clast
1	Uniform enhare	Denosition	rate Fast	shape Sphere	phi 0	distribution	coeff. 0.77	vol % 40.38	21,91
1 2	Uniform sphere Uniform sphere	Deposition Re-	N.A.	Sphere Sphere	0	Uniform Uniform	0.77	36.39	21,91
2	shake	arrangement	N.A.	Spriere	U	Uniform	0.10	36.39	21,91
3	Angle of repose	Deposition	Slow	Micro-	1.5	WIPP ROM	0.77	N.A.	16,13
3	Aligle of Tepose	Deposition	Slow	CT	1.5	Sieve	0.77	IN.A.	10,13
4	Benchmark R0	Deposition	Slow	Micro-	1.5	WIPP ROM	0.77	35.36	38,00
-	Deficilitiankino	Deposition	Stow	CT	1.5	Sieve	0.77	33.30	30,00
5	Benchmark R1	Deposition	Fast	Micro-	1.5	WIPP ROM	0.77	37.00	36,85
•	20110111111111111111	20000		CT		Sieve	0177	07100	00,00
6	Benchmark R2	Deposition	Fast	Micro-	1.5	WIPP ROM	0.77	38.60	41,36
				CT		Sieve			,
7	Benchmark R3	Deposition	Fast	Micro-	1.5	WIPP ROM	0.77	36.42	41,41
				CT		Sieve			'
8	Benchmark R4	Deposition	Fast	Micro-	1.5	WIPP ROM	0.77	37.25	39,43
				CT		Sieve			1
9	Benchmark R5	Deposition	Fast	Micro-	1.5	WIPP ROM	0.77	34.06	39,56
				CT		Sieve			
10	R4 shake	Re-	N.A.	Micro-	1.5	WIPP ROM	0.77	33.55	39,43
		arrangement		CT		Sieve			
11	R4 shake m 0.10	Re-	N.A.	Micro-	1.5	WIPP ROM	0.10	23.51	39,43
		arrangement		CT		Sieve			
12	WIPP very well	Deposition	Fast	Micro- CT	0.175	Log-normal	0.77	47.75	31,77
13	WIPP moderately well	Deposition	Fast	Micro- CT	0.605	Log-normal	0.77	45.53	36,59
14	WIPP poorly	Deposition	Fast	Micro- CT	1.5	Log-normal	0.77	37.37	82,45
15	Sphere very well	Deposition	Fast	Sphere	0.175	Log-normal	0.77	37.49	19,75
16	Sphere moderately well	Deposition	Fast	Sphere	0.605	Log-normal	0.77	32.70	29,30
17	Sphere poorly	Deposition	Fast	Sphere	1.5	Log-normal	0.77	27.51	71,69
18	Rubble sphere	Deposition	Fast	Sphere	1.5	WIPP ROM Sieve	0.77	26.50	48,62
19	R3 - omit finest	Deposition	Fast	Micro-	1.5	WIPP ROM	1.00	35.36	23,97
	clasts µ 1.00			CT		Sieve			1
20	R3 - omit finest	Deposition	Fast	Micro-	1.5	WIPP ROM	0.77	33.75	23,97
	clasts µ 0.77			CT		Sieve			
21	R3 - omit finest	Deposition	Fast	Micro-	1.5	WIPP ROM	0.62	32.74	23,97
	clasts µ 0.62			CT		Sieve			
22	R3 - omit finest clasts µ 0.50	Deposition	Fast	Micro- CT	1.5	WIPP ROM Sieve	0.50	32.36	23,97
23	R3 - omit finest clasts µ 0.25	Deposition	Fast	Micro- CT	1.5	WIPP ROM Sieve	0.25	29.53	23,97
24	R3 - omit finest clasts µ 0.01	Deposition	Fast	Micro- CT	1.5	WIPP ROM Sieve	0.01	24.41	23,97

Lander, et al. Page 11 of 28

2.2.4. Deposition rate

To evaluate whether the rate of clast deposition impacts the porosity and internal structure of the simulated rubble pile, we considered two alternative scenarios involving the rate of clast deposition. In the case involving the "Slow" entry under "Depositional rate" in **Table 2**, a deposition event began with the placement of a clast at a specified vertical distance (10 cm in this study) above the top of the pack where it falls under the influence of gravity. New clasts were not introduced into the physics scene unless the cumulative kinetic energy of all clasts in the scene was below a specified threshold. The "slow" deposition simulation in this study was configured such that there are generally fewer than 50 freefalling objects at a time.

In simulations with a "Fast" "Depositional rate" in **Table 2**, all clasts were placed above the container floor such that the first clast in the deposition schedule was nearest to the bottom of the container and the vertical positions of remaining clasts were moved upwards as needed such that no clasts overlapped. The clasts were then dropped under Earth's gravity. With this approach, many more clasts undergo impact simultaneously as deposition proceeds. Clast velocities may not exceed terminal velocities calculated by Stoke's law of settling (53), assuming a spherical particle shape and the viscosity and density of air.

2.2.5. Deposit rearrangement simulations

Induced clast rearrangement associated with the impact of large clasts or earthquakes can cause pack porosity values to decrease. In this study rearrangement simulations used the final state of deposition simulations or previously simulated rearrangement simulations as a starting point. These simulations are indicated by "Rearrangement" in the "Run Type" column in **Table 2**.

Clast rearrangement was induced using repeated combinations of three types of events: piston drop, vertical shaking, and horizontal shaking. For piston drop events, a piston, which has a diameter slightly less than that of the interior of the container, was introduced at a specified height above the pack and released. Shake events involved moving the container a specified distance at a defined speed either vertically or in a randomly selected horizontal direction. The container was then returned to its starting point using the same speed.

A rearrangement event concluded when the combined kinetic energy of the pack clasts drops below a specified threshold value. In some cases, as discussed in section 3.3.2, clast frictional coefficients were reduced to promote greater magnitudes of porosity loss in response to rearrangement events.

3. RESULTS

3.1. WIPP run of mine clast size distribution and shapes

Sieve analysis of WIPP ROM material that passed through ~76 mm screen openings (**Table 1**) reveals a broad range in clast sizes (**Fig. 3**). Over 50 wt% of the clasts fall within a sieve opening range of ~5–38 mm while less than 2 wt% of the mass passed through a 1 mm sieve opening. The mass averaged mean clast size is 12.7 mm and the mass weighted clast size variation in standard deviation in phi units (**Eq. 1**) is 1.5. We also assessed the size distribution using the Trask sorting coefficient (66) (**Eq. 2**), where P75 is the 75th mass percentile and P25 is the 25th mass percentile of the clast size distribution in mm.

$$T = \sqrt{\frac{P75}{P25}}$$
 (2)

This measure, T, of the clast size variability has a value of 2.2, and, like the standard deviation in phi of 1.5, is comparable to "poorly sorted" sedimentary deposits (16, 60).

Clast shapes are highly variable across a broad range in sizes (Fig. 4, Fig. 5, Fig. 6, Fig. 7). Most of the clasts have irregular surfaces and platy or elongated forms. We find that an estimated minimum sieve

Lander, et al. Page 12 of 28

opening size based on an analysis of the clast shape provides a better correspondence to the opening range for sieve separates compared to the long axis of the clast. This estimate is obtained by rotating a clast surface mesh through a range of orientations while determining the minimum size that it can pass

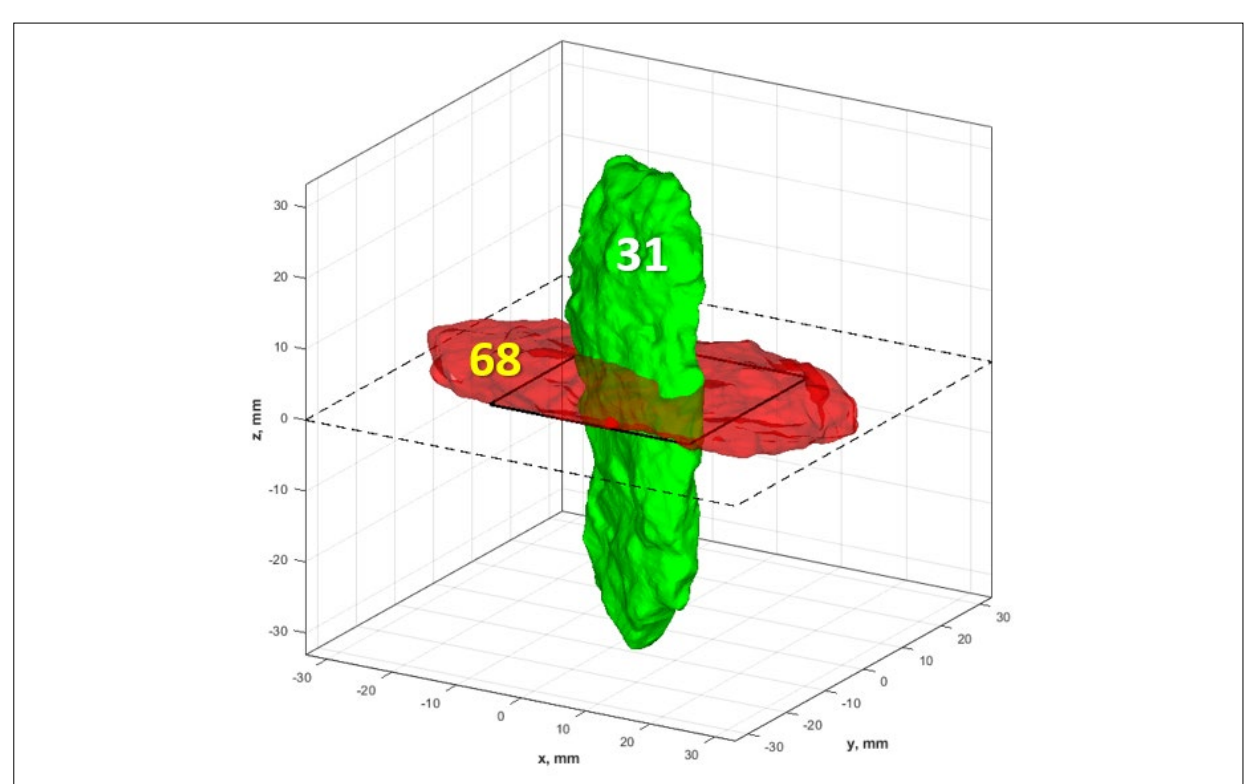


Figure 9: The minimum sieve opening size a clast can pass through is estimated as the smallest square that a clast can pass through by translating in a direction perpendicular to a square. This clast has a long axis length of 68 mm, but was obtained from the 19 to 38 mm sieve size separate. The estimated minimum sieve pass through size for the clast is 31 mm, which is consistent with the sieve size fraction. The orientation of the clast for this estimated size opening is shown by the green color where the sieve opening is indicated as the square drawn with a black, solid line that lies in the x / y plane. The orientation shown by the red color shows the least favorable minimum sieve opening size, which is 68 mm and is indicated by the dashed square in the x/y plane.

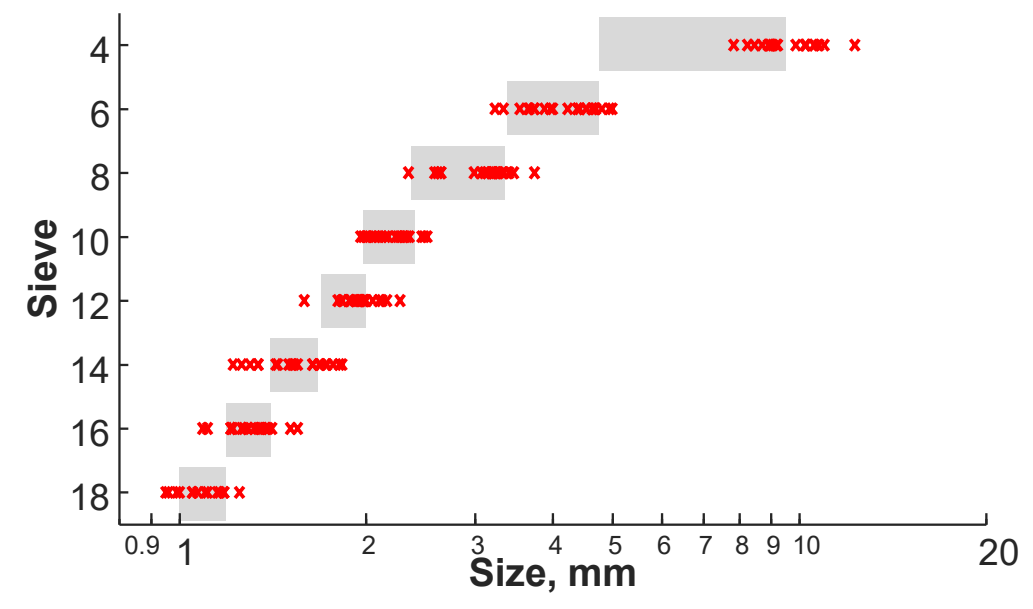


Figure 10: A comparison between the sieve fraction opening sizes as shown by the thick black lines and the estimated minimum sieve pass through size for associated clast shapes (red "X" symbols).

Lander, et al. Page 13 of 28

through by translation in a direction perpendicular to the plane of a square that represents a sieve opening size (**Fig. 9**). The analysis is simplistic in that it does not consider the potential for clasts to rotate or translate in other directions as they pass through the square opening. Thus, for example, the minimum opening size a clast could pass through would be overestimated for a banana-like shape. Nonetheless, ~95% of the estimated minimum sieve opening sizes are within 10% of the sieve opening range for the characterized clast shapes (**Fig. 10**).

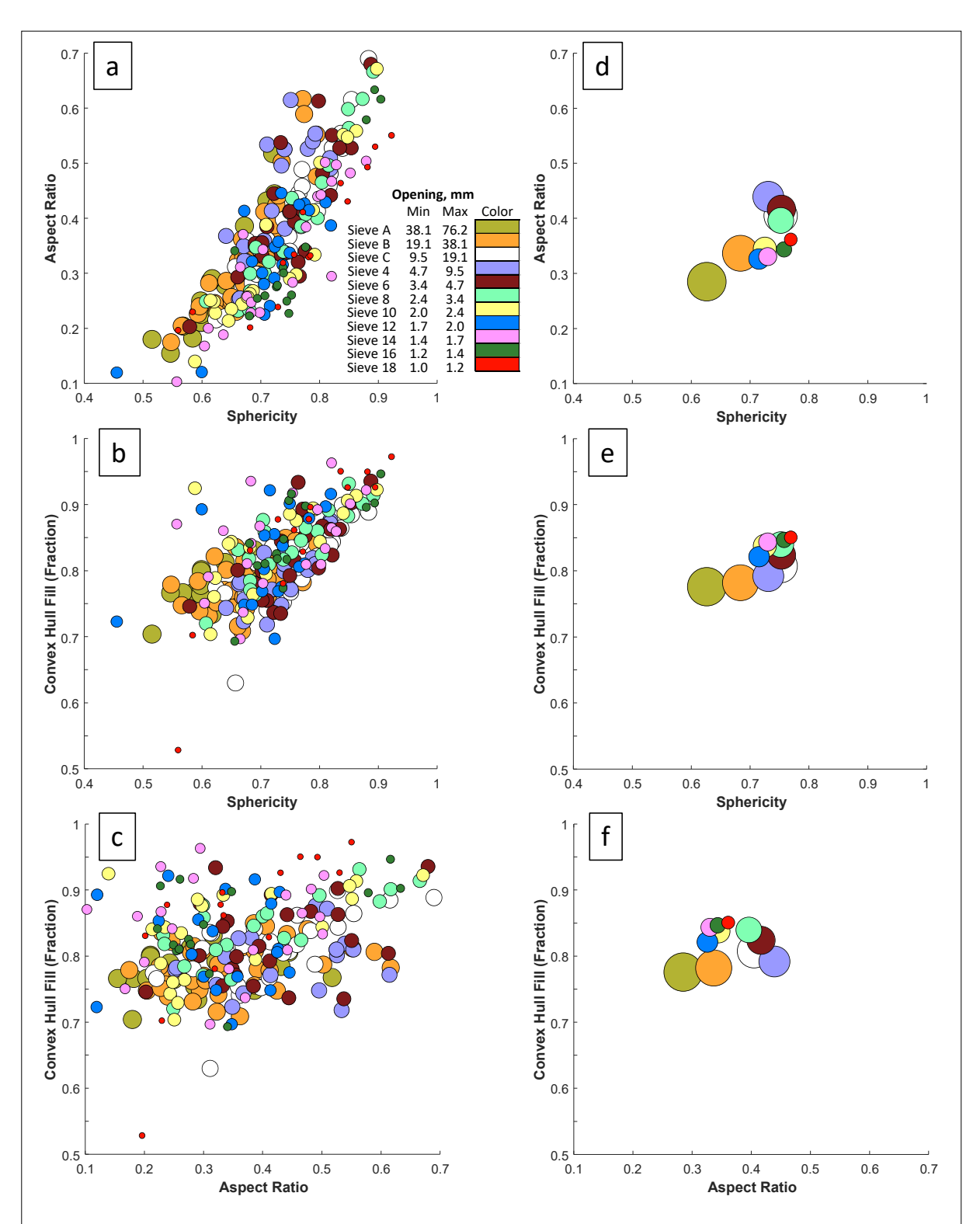


Figure 11: Clast shape metrics where symbols are sized and color coded by sieve fraction (see legend in **(a)**). The left column of plots shows measurements made on individual clasts whereas the right column shows averages by sieve fraction.

Lander, et al. Page 14 of 28

We determined three shape metrics for each scanned clast: 1) *sphericity* (the ratio of the surface area of an equivalent volume sphere to the actual surface area), 2) *aspect ratio* (the ratio of the minimum Feret diameter (15) to the long axis), and 3) *convex hull fill fraction* (the ratio of clast volume to the volume of a convex hull around the clast). The first two of these metrics are measures of the overall clast form where lower values correspond to greater departures from spherical shapes. The last metric, on the other hand, is an indication of the extent to which the clast surface is characterized by pits and embayments, with lower values indicating greater departures from convex forms.

In **Figure 11**, these metrics are plotted against each other where the symbols are color coded and sized by sieve size fraction. The clasts exhibit a wide range of shapes as defined by these metrics, even within a given sieve size fraction. There is a tendency, however, for clasts in the 2.4–19.1 mm size range to have greater sphericity and larger aspect ratios compared to other sizes. Thus, these clasts generally are more equant compared to smaller or larger clasts. Clasts >19.1 mm in size, on the other hand, have the lowest sphericities, aspect ratios, and convex hull fill fractions. These clasts therefore tend to have more irregular shapes and rougher surfaces compared to smaller clasts.

3.2. Simulation tests

We conducted two types of tests of the simulation method to evaluate its performance. The first of these tests involves porosity values for uniform packings of spheres and the second considers angles of repose.

3.2.1. Monodispersed sphere packs

A deposition simulation involving ~22,000 clasts with a frictional coefficient of 0.77, has an interclast porosity of 40.4 vol% (run 1 in **Table 2**, **Fig. 12a**). This porosity value is within the measured range of 40 to 41 vol% for "loose random packing", that is obtained by gently dropping spheres into a container (24).

Using this depositional pack as a starting point, we induced rearrangement through container shaking while also reducing the frictional coefficient to 0.1. The resulting pack has an interclast porosity value of 36.4 vol% (run 2 in **Table 2**, **Fig. 12b**). This value falls within the 35.9 to 37.5 vol% range for "close random packing" that is observed after vibrating or shaking uniform sphere deposits in the laboratory (24).

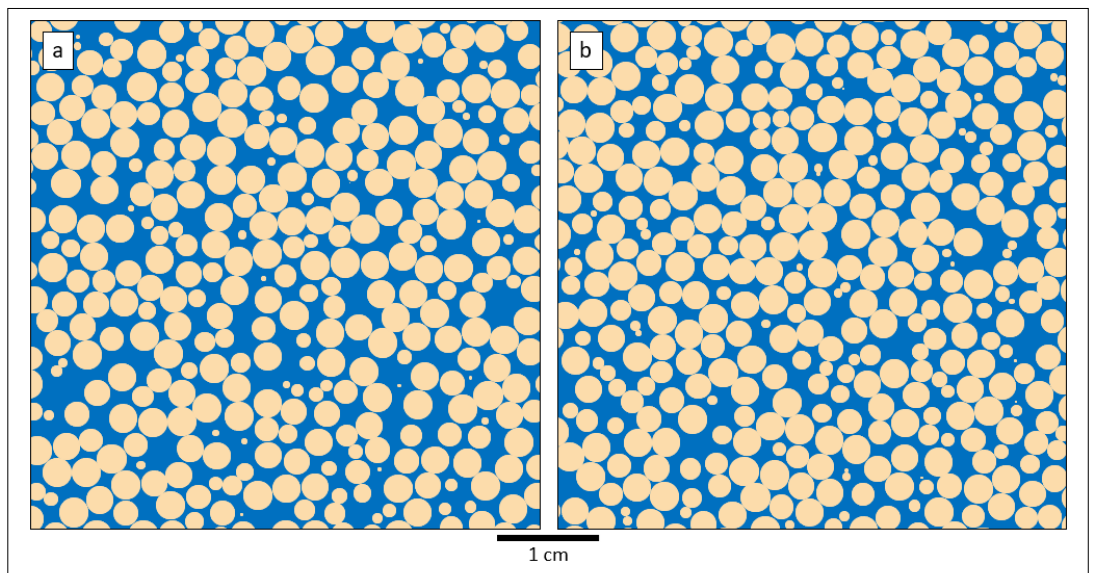


Figure 12: Vertical cross sections through simulated 3D packs of spheres with uniform diameters of 2.88 mm. The packs have been trimmed to 5 cm cubes taken from the center of the deposited volumes. **(a)** Deposition with no shaking and a frictional coefficient of 0.77 (run 1 in **Table 2**). This pack has an interclast porosity of 40.4 vol%. **(b)** After rearrangement from shaking with a frictional coefficient of 0.1 (run 2 in **Table 2**). This pack has an interclast porosity of 36.4 vol%.

Lander, et al. Page 15 of 28

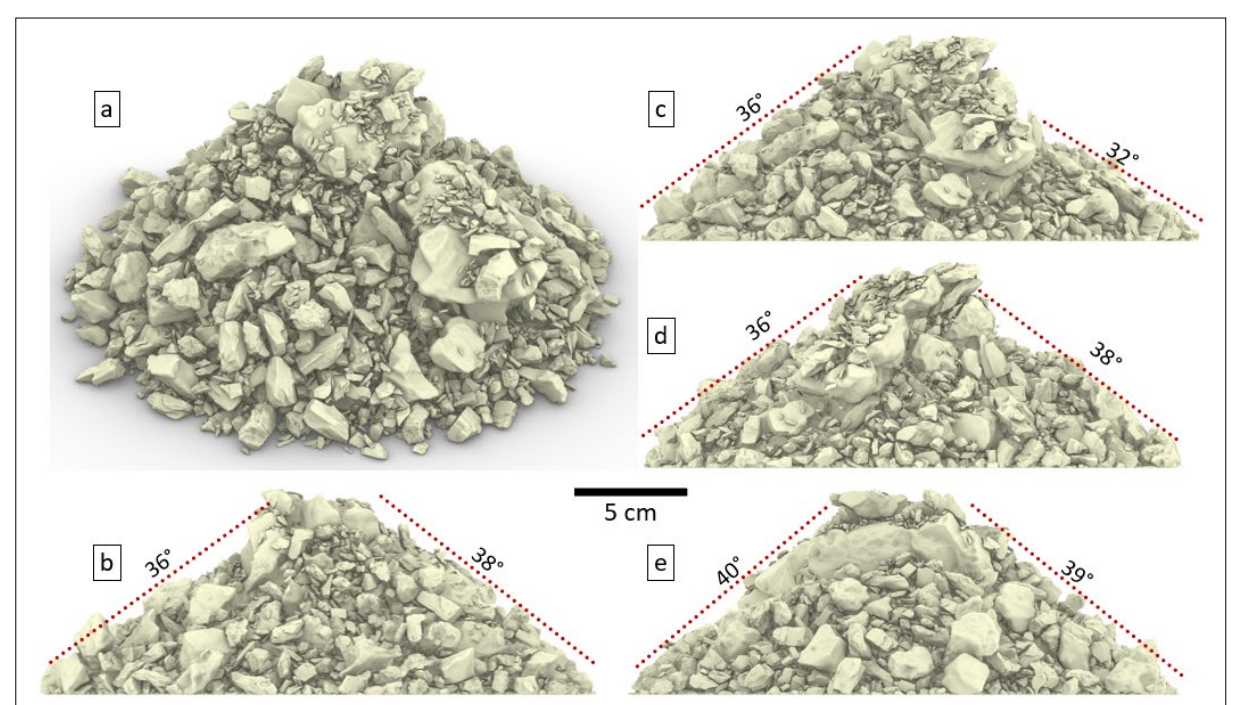


Figure 13: Several views of an angle of repose simulation together with estimated slope values. The simulation uses dynamic and static frictional coefficients of 0.77 and WIPP ROM size distribution and shapes. The starting point for the simulation is the pack from run 7, which includes ~41,000 clasts (**Table 2**). **(a)** Oblique view. **(b-e)** Side views from various positions.

3.2.2. Angle of repose

Friction is an important control on the porosity and internal microstructure of granular materials (13). The angle of repose of WIPP ROM material provides a useful constraint on frictional properties, although other factors such as clast shape may affect the angle of repose (2).

Crushed salt is commonly reported to have an angle of repose of 30° (e.g. 37), but our measurements on piles of ROM salt at the WIPP site range from 35–40°. We also created a ~30 cm high pile in the laboratory using WIPP ROM material with clasts <4 cm in size and measured a range in angles of repose of 32–41° (n = 8). By Coulomb's theory (1), the frictional coefficient may be estimated as the tangent of the angle of repose. Thus, based on these observations, we set the static and dynamic coefficients of friction for clasts in our angle of repose simulations of WIPP ROM material to be 0.77, which is the tangent of 37.5°. We used two alternative methods for these simulations. In one we used the "slow" depositional process described in section 2.2.4 where the clasts were dropped from the same x-y position (run 3 in **Table 2**), and in another we simulated the collapse of a rubble deposit by removing the container annulus from the end results of run 7 (**Fig. 13**). In each simulation the angles of repose range from 32–40°, which was in good agreement with the measurements.

Although the frictional properties of clasts are an important control on the angle of repose, clast shape and size distribution also are important factors, as illustrated in **Figure 14** where all simulations used the same uniform clast size of 2.88 mm (minimum sieve opening) and dynamic and static frictional coefficients of 0.77, but with different shapes. By Coulomb's theory, this frictional coefficient value should result in an angle of repose of 37.5°. The sphere pile, however, has an angle of repose of ~27° whereas the cube pile is ~43°. The pile using micro-CT shapes from the sieve 8 fraction of ROM material comes closest to the expected angle of repose with a slope of 40°, which is on the upper end of the range for the simulation using the full range of the ROM clast sizes and shapes (**Fig. 13**). These results demonstrate that sphere packings are unlikely to accurately reproduce ROM rubble properties.

Lander, et al. Page 16 of 28

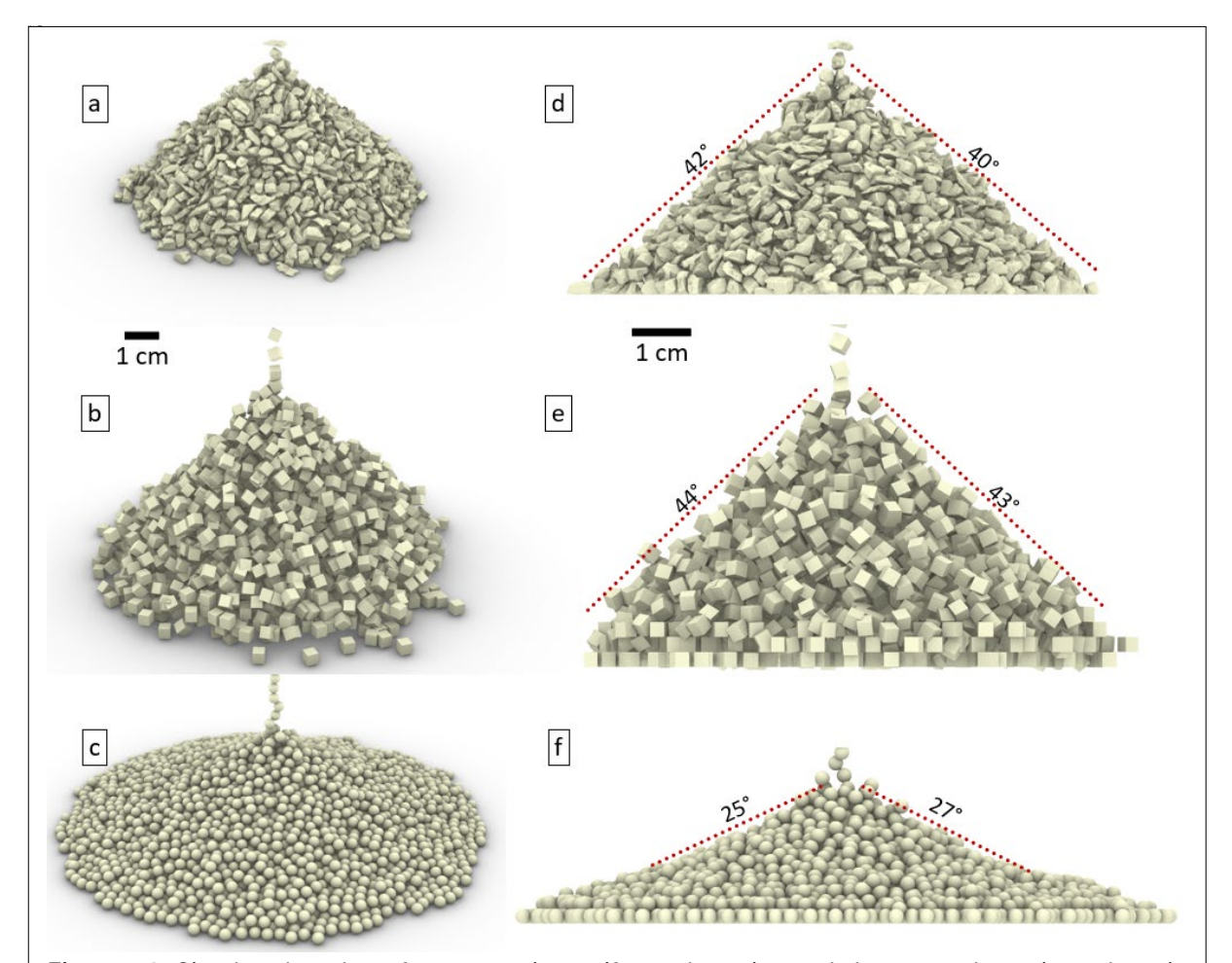


Figure 14: Simulated angles of repose using uniform clast size and the same dynamic and static frictional coefficient of 0.77, but differing clast shapes, where the left column shows an oblique view and the right column shows a side-on view: (a) & (d) micro-CT shapes from sieve 8 size separates (Fig. 6), (b) & (e) cubes, & (c) & (f) spheres.

3.3. Rubble deposit simulations

In the simulation of the porosity and internal structure of rubble deposits, we investigated the stochastic variability in results, the influence of induced rearrangement, and the effect of variations in the shapes, size distributions, and frictional coefficients of clasts.

3.3.1. Benchmark packs

Our benchmarks in the assessment of pack internal structure and porosity are deposition simulations that consider the sieve size distributions from the WIPP ROM sample (**Table 1**, **Fig. 3**), micro-CT derived clast shapes from this material (**Fig. 4**, **Fig. 5**, **Fig. 6**, and **Fig. 7**), frictional coefficients of 0.77 (see section 3.2.2), and deposition into a vertically oriented cylindrical container with a 12 cm interior diameter. We conducted six such simulations using alternative random number seeds (runs 4–9 in **Table 2**). Approximately 40,000 clasts were considered in each simulation (**Fig. 3**). The largest sieve size fraction, which makes up ~8 mass% of the size distribution, was represented by just one clast in each of the realizations. By contrast, ~16,000 clasts were used for the smallest size fraction, which represents ~2 mass% of the size distribution.

We extracted a cube with 8 cm edge lengths (512 cm³ volume) from each pack and obtained a range in porosity values of 34.1–38.6 vol% (**Table 2**, **Fig. 15**, **Fig. 16**). These porosity values are lower than two laboratory measurements on packs made using WIPP ROM material of 40.2 and 42.5 vol% (3). Sieve analysis indicates that the clast size distributions for these experiments, however, differ from those considered in the benchmark simulations.

Lander, et al. Page 17 of 28

The porosity value for a benchmark simulation with the "slow" depositional rate (run 4) falls within the range of benchmark simulations with "fast" rates (runs 5-9), suggesting that the variations in depositional rate considered in the analysis have limited impact on simulation results.

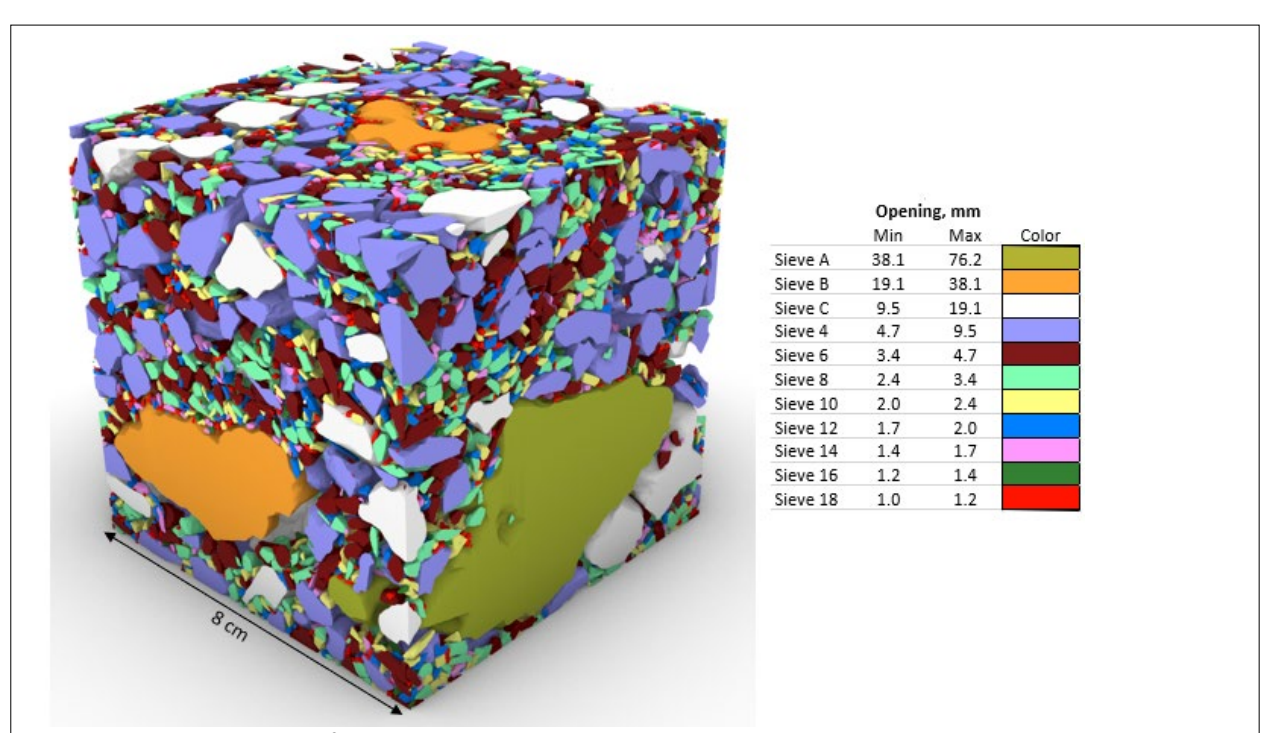


Figure 15: Cube (512 cm³) extracted from a "benchmark" simulation (run 5). The clasts are colored by sieve fraction as indicated in the legend.

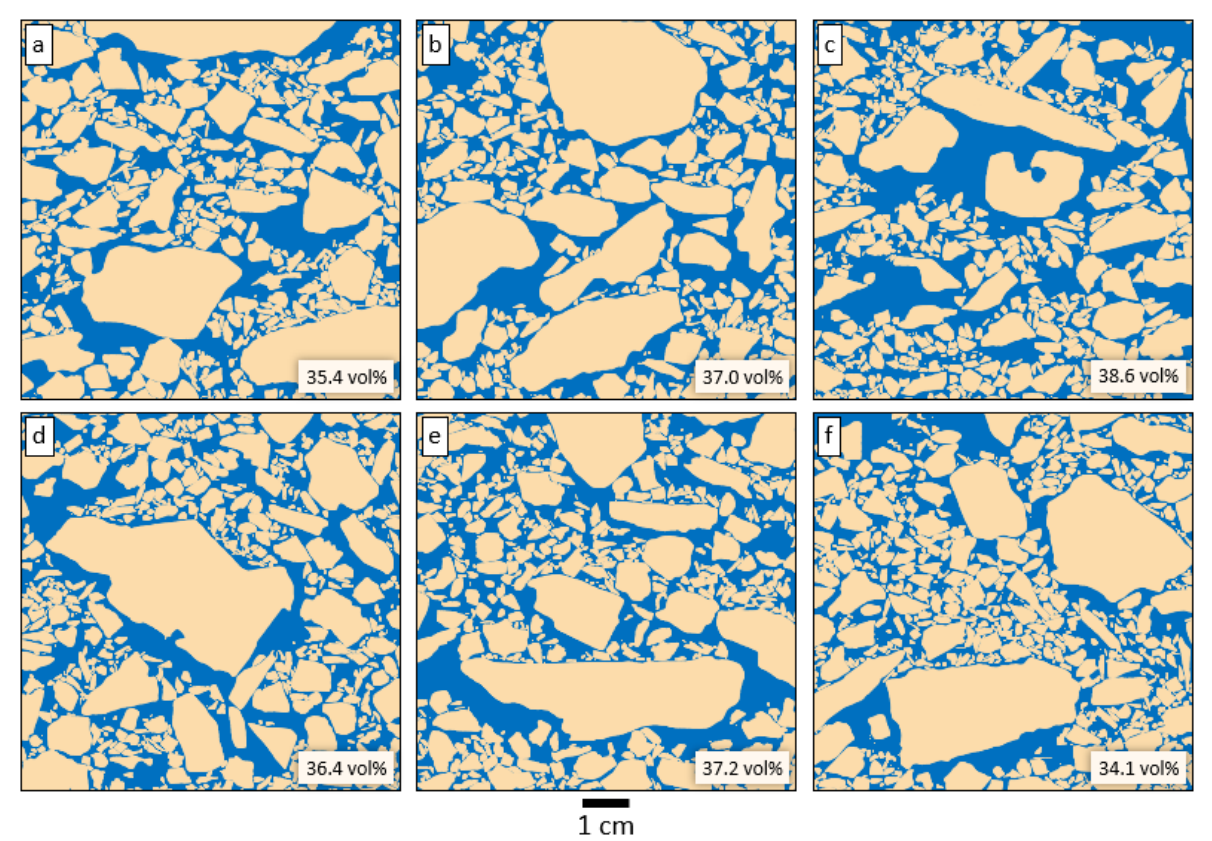


Figure 16: Vertical cross sections through benchmark simulations of WIPP ROM rubble deposit. Run information is provided in **Table 2.** (a) run 4, (b) run 5, (c) run 6, (d) run 7, (e) run 8, & (f) run 9. Interclast porosity from a 512 cm³ cube volume is indicated in the lower right corner of each image.

Lander, et al. Page 18 of 28

The standard deviation in porosity for the benchmark simulations of 1.6 vol% has a 95% confidence interval ranging from 1.0 to 3.9 vol% for the six measured values based on the chi-squared distribution (39). While increasing the number of simulations would reduce the uncertainty in the analysis, these results demonstrate limited variability in porosity among the simulations.

3.3.2. Effect of induced clast rearrangement

We assessed the potential magnitude of porosity loss by clast rearrangement using one of the benchmark packs as a starting point. Such rearrangement could be induced by the impact of boulders or large slabs falling on the top of rubble piles during room collapse or by earthquakes. The simulated porosity decreased from an initial value of 37.0 (run 5 in **Table 2**) to 33.6 vol% (run 10 in **Table 2**) in response to piston drop and shaking events, while maintaining a constant frictional coefficient of 0.77 (**Fig. 17a** and **b**). This 3.4 vol% porosity reduction is consistent with laboratory induced rearrangement

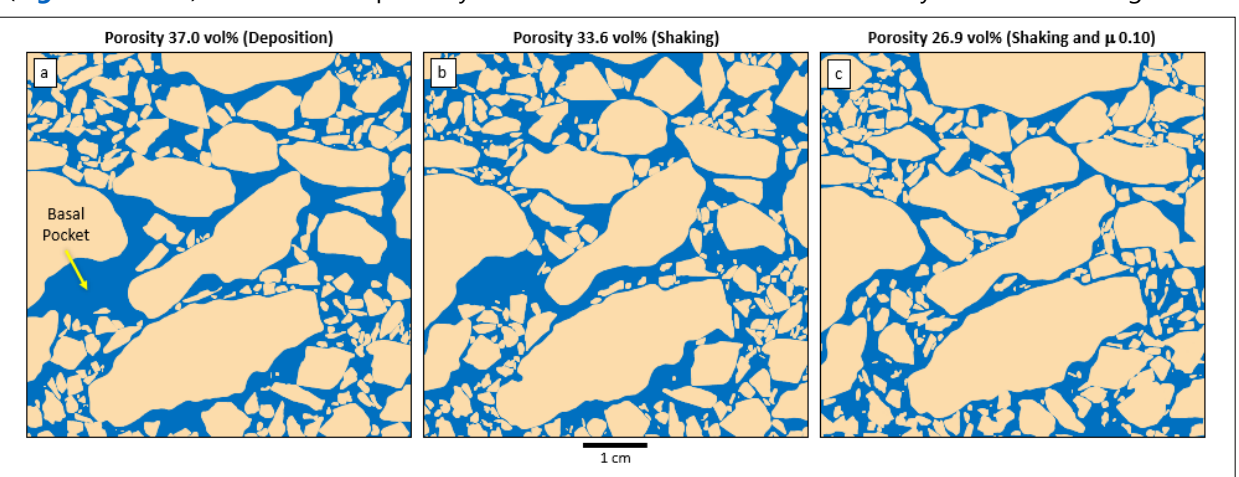


Figure 17: Impact of clast rearrangement: vertical cross sections. (a) Geometry after deposition but before shaking using a frictional coefficient of 0.77 (run 5 in Table 2). (b) Geometry after the simulation from (a) was subjected to repeated clast rearrangement events using frictional coefficients of 0.77 (run 10). (c) Geometry after the simulation from (b) was subjected to repeated clast rearrangement events and the frictional coefficients were lowered to 0.1 (run 11). Note how the size of large pore ("basal pocket") beneath large clasts (yellow arrow) in (a) has been reduced in (c).

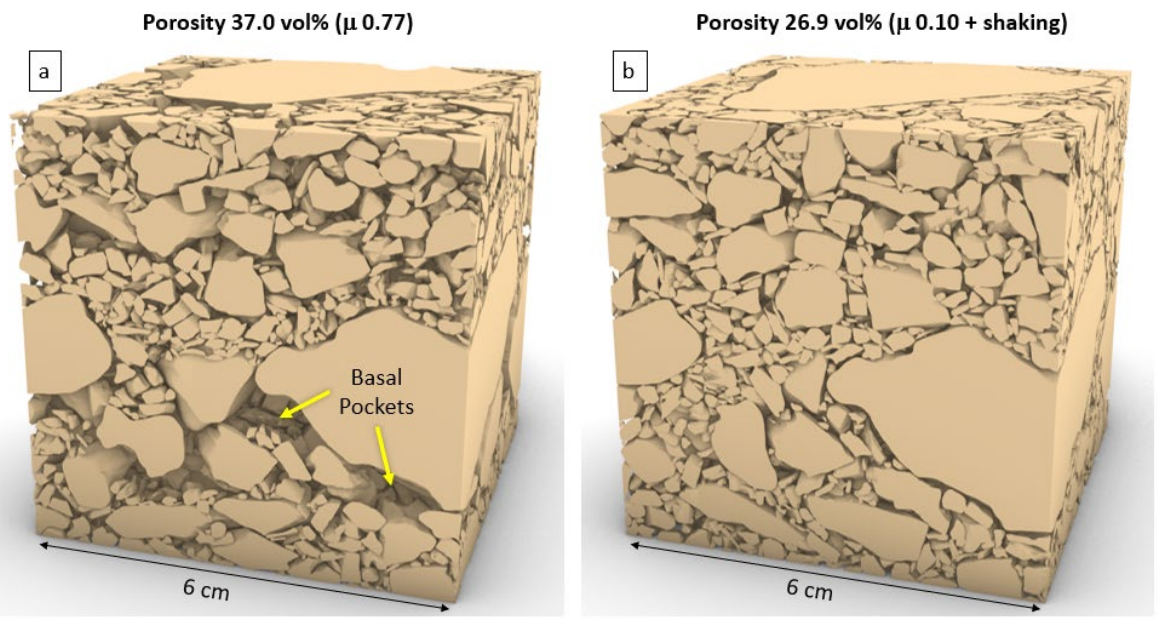


Figure 18: Impact of clast rearrangement: 3D volumes. (a) Geometry after deposition without shaking and using frictional coefficients of 0.77 (run 5 in Table 2). (b) Geometry after the result in (a) was subject to repeated induced rearrangement events and the frictional coefficients were decreased to 0.1 (run 11). Note how the size of large pores ("basal pockets") beneath large clasts (yellow arrows) in (a) have been reduced in (b).

Lander, et al. Page 19 of 28

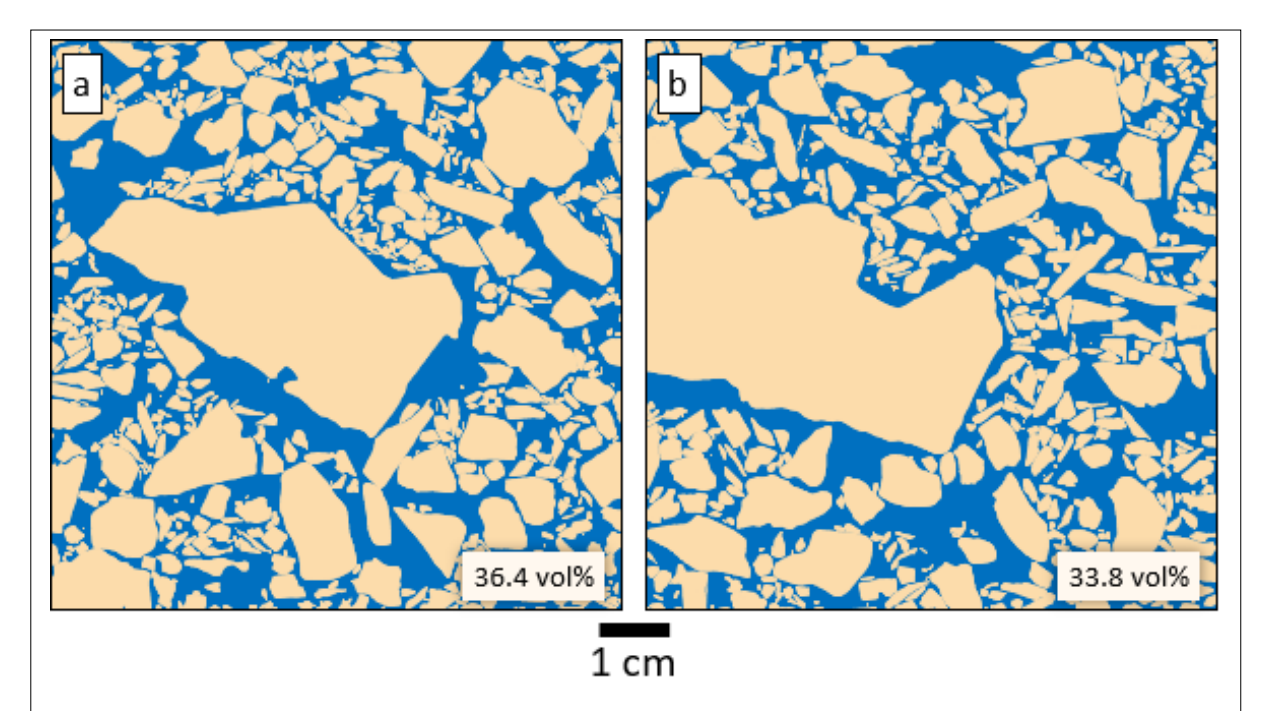


Figure 19: Vertical cross sections through 3D packs illustrating the effect of omitting the smallest clast size fraction. (a) Benchmark run 7, & (b) run 20, which uses the same deposition schedule apart from omitting clasts < 1.19 mm in size, which represent \sim 2% of the volume and \sim 40% of the number of clasts. (See Table 2 for run configurations.)

of WIPP ROM packs, which resulted in an average porosity drop of 3.1 vol% in experiments by Babcock (3).

We conducted an additional rearrangement simulation with the objective of assessing the maximum potential porosity loss from this process. To facilitate clast movement, we reduced the frictional coefficients from 0.77 to 0.1 (a value comparable to talc) prior to inducing additional piston drop and shaking events for the pack that resulted from the first rearrangement simulation. These steps resulted in an additional 6.7 vol% porosity loss through clast rearrangement (run 11 in **Table 2**, **Fig.17c**). The resulting interclast porosity of 26.9 vol% likely is approaching the minimum potential value for this simulation configuration in the absence of clast deformation or breakage.

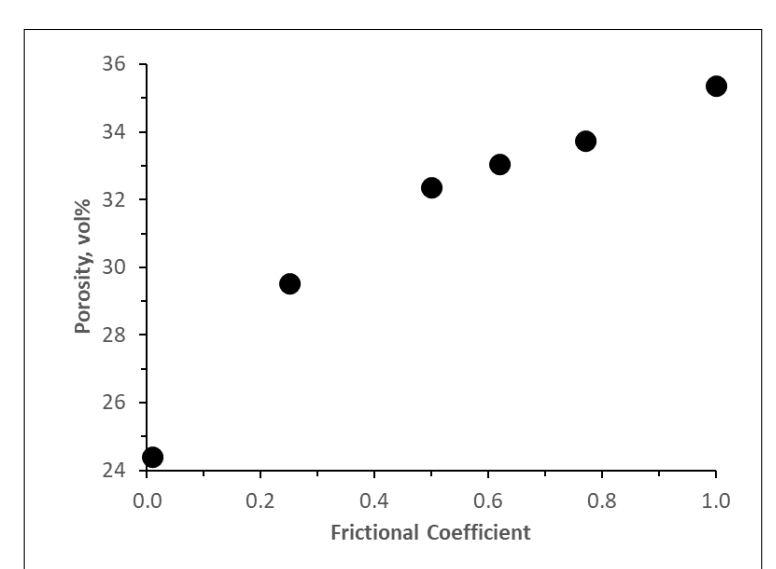


Figure 20: Influence of frictional coefficient on interclast porosity. All simulations use the same depositional schedule but different friction values (runs 19—24 in Table 2).

One significant mechanism contributing to porosity loss during clast rearrangement involves the filling of "basal pocket" pores that occur beneath large clasts (Fig. 17a, Fig. 18a). These pockets develop during deposition as larger clasts shield the pores beneath them from being filled by smaller clasts subsequently deposited from above. Clast rearrangement, however, allows smaller clasts to move into these voids.

3.3.3. Effects of finest clast size fraction and friction

Although the finest size fraction of the WIPP ROM size distribution (<1.19 mm) makes up only ~2 vol% of the mass, it constitutes ~40% of the

Lander, et al. Page 20 of 28

number of clasts used in the simulations. To assess the impact of these small clasts on simulated porosities, we conducted a simulation that was identical to one of the benchmark configurations apart from omitting these small clasts (**Fig. 19**). We found that the simulated interclast porosity values are similar: 33.8 vol% for the run lacking the small clasts (run 20 in **Table 2**) compared to 36.4 vol% for the run that included them (run 7 in **Table 2**).

Due to the significantly reduced simulation time of the depositional schedule that omits the finest clasts, we used this configuration as the basis for evaluating the sensitivity of deposition results to clast frictional properties. Interclast porosity values vary systematically from 24.4 to 35.4 vol% with frictional coefficients ranging from 0.01 to 1.00 (**Fig. 20**, runs 19–24 in **Table 2**). Porosity values decrease rapidly as the friction coefficient drops below 0.5. The change in porosity for frictional coefficients between 0.62 and 1.00, however, is only 2.3 vol%, which is less than the 3.2 vol% range shown by the benchmark simulations with statistically equivalent input configurations. As discussed in section 3.2.2, frictional coefficients for salt clasts derived from angles of repose range from ~0.58 to 0.77. Thus, rubble porosity values appear to be relatively insensitive to frictional values within the range of uncertainty associated with halite.

3.3.4. Effect of clast size distribution and shape

"Polydispersity" (i.e., variations in clast sizes) in clastic deposits reflects the material's origin, transport, and deposition history. For instance, clastic sediments often display lognormal size distributions (16, 45, 60), whereas the sizes of blasted and crushed-rock fragments are commonly described using Weibull distributions (48).

A measure of polydispersity is the standard deviation in phi units (**Eq. 1**). To evaluate the impact of polydispersity on porosity, we considered simulations that use log-normal size distributions with standard deviations in phi of 0.18, 0.60, and 1.50, which represent very well sorted, moderately sorted, and

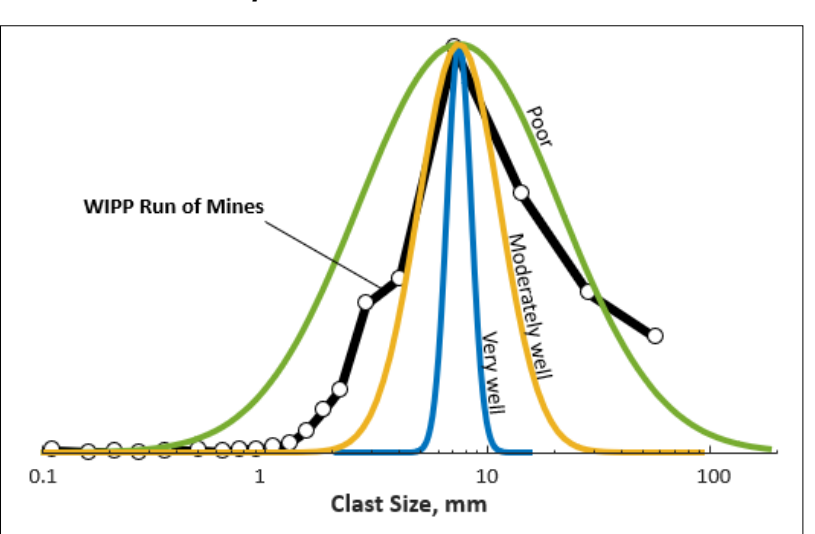


Figure 21: Comparison of the volume-weighted size distribution from sieve analysis of WIPP ROM material with log-normal distributions with standard deviations in phi units of 0.18, 0.60, and 1.5, consistent, respectively, with the very well, moderately well, and poorly sorting classes of Folk (17).

poorly sorted classifications, respectively (16, 60). We compare the associated size distributions with the sieve-derived distribution for WIPP ROM material in **Figure 21**. The ROM size distribution, like the poorly sorted distribution (green line in **Fig. 21**), has a standard deviation in phi of 1.5.

In the simulations, we considered the effect of clast shape on porosity and internal structure by contrasting results obtained using micro-CT derived forms from the WIPP site (runs 12-14 in **Table 2**) with those obtained using spheres (runs 15-17 in **Table 2**). Results for packs with both types of clast shapes show systematic decreases in interclast porosity as polydispersity increases (**Fig. 22**, **Fig. 23**). The trends from these simulations are similar to those shown by data from laboratory experiments on quartzrich sand packs by Parker et al. (44) that have medium and coarse mean clast sizes (0.39 and 0.65 mm, respectively). The magnitude of the porosity decline for a given clast shape is ~10 vol% from the very well to the poorly sorted simulations. This loss in porosity with increasing polydispersity occurs in response to two end-member factors as illustrated in **Figure 24**. Porosity decreases when a region populated with smaller clasts and associated interstitial pores is replaced by a large solid clast and when the interstitial pores between large clasts are partially filled by small clasts.

Lander, et al. Page 21 of 28

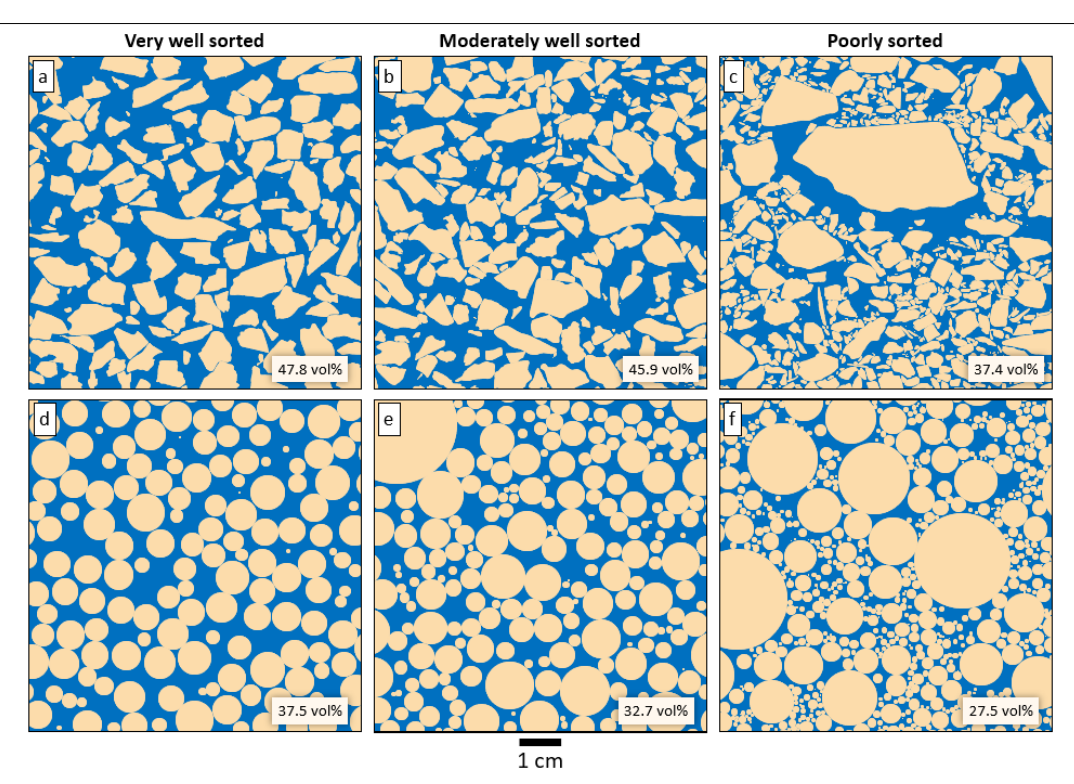


Figure 22: Vertical slices from 3D simulations with the same mean clast size of 7.4 mm but with three different log-normal size distributions (see Fig. 21). WIPP ROM clast shapes are used for: (a) run 12, (b) run 13, & (c) run 14, whereas spheres are used for (d) run 15, (e) run 16, & (f) run 17. Interclast porosity from the volume is indicated in the lower right corner of each image. See Table 2 for run configurations.

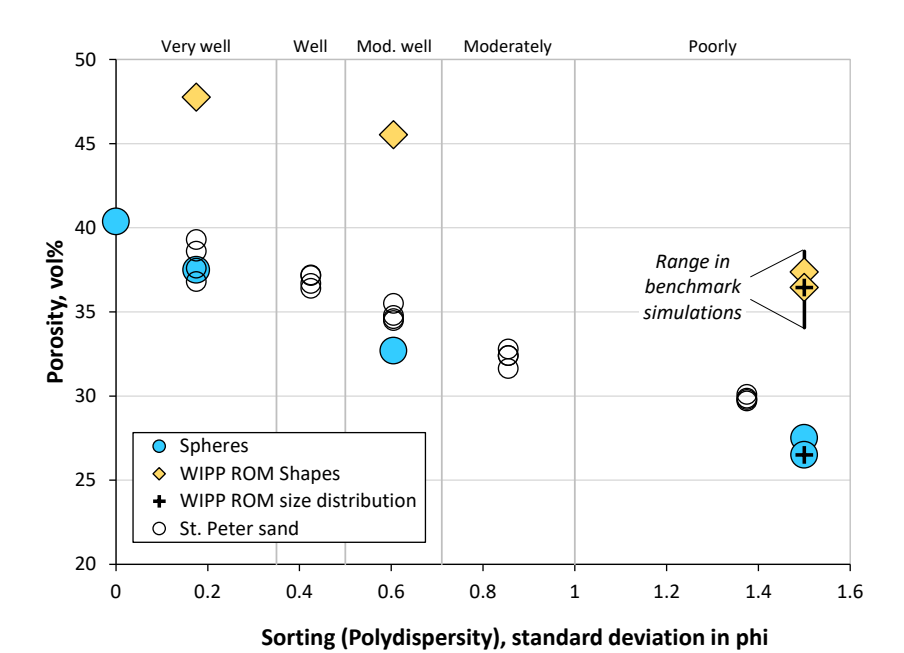


Figure 23: Dependency of pack interclast porosity on the clast size distribution and shape. Simulated values with clast shapes from micro-CT analysis of WIPP ROM clasts (diamonds) are compared with simulations using sphere shapes (blue circles). Additionally, experimental data (open circles) are shown for well-rounded quartz-rich sand packs from Parker et al. (44). All data employ log-normal clast size distributions with the exception of the points indicated with "+" symbols that use the sieve-derived size distribution for WIPP ROM material. Sorting classifications are shown for reference along the top of the plot (16, 60).

Lander, et al. Page 22 of 28

The sphere pack results have similar porosities to the quartz sand experiments, although they tend to have somewhat lower values (Fig. 23). The clasts in the sand experiments are well rounded with smooth surfaces (44), and therefore have forms that are much closer to spheres compared to the irregular shapes of WIPP ROM clasts. Simulations involving ROM clast shapes have porosities that are ~10–13 vol% higher compared to otherwise equivalent runs made using spheres. For example, the moderately well sorted simulation with ROM shapes has an interclast porosity of 45.9 vol% (run 13 in Table 2) compared to 32.7 vol% for an otherwise equivalent simulation made using spheres (run 16 in Table 2). Compared to contacts among spheres, ROM clasts are more likely to have rough surfaces that impede movement into tighter packing arrangements. Additionally, interclast porosity increases when packs include clasts that have concave regions that are too small to allow for a single surface contact with a neighboring clast.

A final consideration involves the impact of the form of the size distribution. The WIPP ROM size distribution and the log-normal poorly sorted distributions both have standard deviations in phi of 1.5, although the former distribution is skewed toward larger clast sizes (Fig. 21). The 38.4 vol% porosity of the simulation that uses log-normal distribution (run 14 in Table 2) falls within the 35.4 – 38.6 range of values for the benchmark simulations that use the WIPP ROM size distribution (runs 4-9 in Table 2). Thus, it appears that the difference in the shape of the size distributions in this case has a far less significant effect on porosity compared to the polydispersity magnitude and clast shape effects discussed previously in this section.

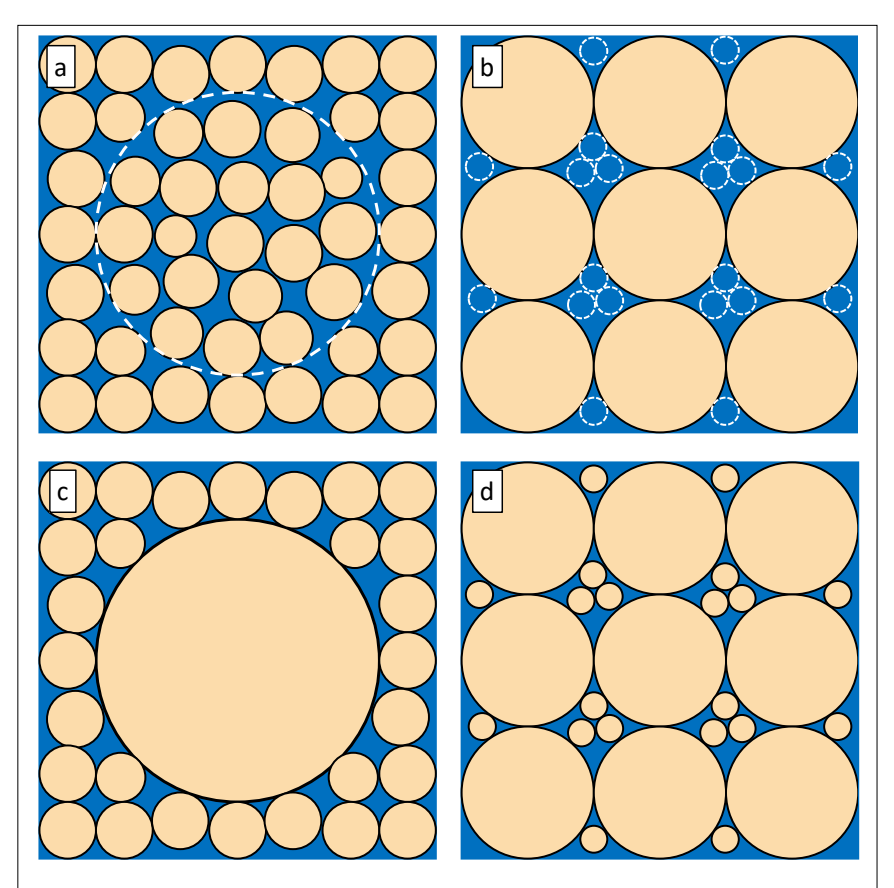


Figure 24: Schematic cross sections illustrating the two end-member factors that lead to decreased interclast porosity with increased clast size variability. Cases (a) and (b) show nearly uniform clast size is associated with high porosity. In (c) a large clast fills a region that in (a) has significant interclast porosity. In (d) small clasts fill interstices between large clasts in (b). The areas with dashed lines in (a) and (b) show regions where porosity is lost in (c) and (b).

Lander, et al. Page 23 of 28

4. DISCUSSION

Interclast porosity values for the benchmark simulations range from 35.4 – 38.6 vol% among six simulated rubble packs. These benchmarks honor WIPP ROM clast size distributions, shapes, and frictional characteristics while considering different stochastic realizations (runs 4-9 in **Table 2**). It is likely that the variability among realizations would decrease in cases involving narrower distributions in clast sizes or where clast shapes have simpler or less variable forms. Conversely, porosity variability may increase if the library of micro-CT-derived clast shapes were expanded beyond the 176 entries considered in the analysis, or for cases involving broader variations in clast sizes.

In a sensitivity analysis, we find that the most important factors affecting simulated depositional porosity and internal structure are variations in clast size distributions, shapes, and frictional coefficients. Results appear to be insensitive to two alternative rates of deposition. The magnitude of porosity loss with increasing polydispersity is ~ 10 vol% for log-normal distributions over the range from very well to poorly sorted (0.2 – 1.5 standard deviation in phi). The rates of porosity decline with increasing polydispersity are similar for simulations with WIPP ROM clast shapes and spheres while also being comparable to laboratory experiments conducted on sand packs. Importantly, however, simulations that incorporate ROM clast shapes have 10 - 13 vol% greater porosity compared to otherwise equivalent simulations involving spheres.

The poorly sorted simulation with a log-normal distribution and the empirical clast size distribution from WIPP ROM salt material both have the same 1.5 magnitude of polydispersity as measured in standard deviation in phi, but with differing distribution shapes and symmetries. The porosity value from the log-normal distribution simulation is within the range for the benchmark simulations. Thus, the overall form of the size distribution for this polydispersity value in these test cases is of much lower significance compared to the range in polydispersity values considered in our analysis.

Pack porosities decrease by ~ 11 vol% as frictional coefficient values decrease from 1.0 to 0.01. Otherwise equivalent simulations with frictional coefficients ranging from 0.62 to 1.0 yield porosity values that differ by only 2.3 vol%. This range in frictional properties exceeds the likely range of uncertainty from halite. Consequently, uncertainties in frictional coefficients within the range of 0.62–1.0 appear to have a minor effect on simulation results.

We found that omitting the smallest size fraction from the WIPP ROM distribution, which represents 2 vol% of the mass and ~40% of the number of simulated clasts, results in a modest 3.4% drop in simulated interclast porosity. These small clasts, however, have the potential to reduce permeability due to their high surface areas and narrow associated pore throats.

Induced rearrangement could be triggered by the impacts of large clasts during room collapse, or by seismic events such as earthquakes. A simulated ~3 vol% decrease in porosity due to clast rearrangement is comparable to values observed in laboratory measurements. We estimate that the maximum potential porosity loss by induced rearrangement in the absence of clast deformation is ~10 vol%. Such large magnitudes of porosity loss by this process, however, are unlikely given that this simulation involved the use of very low frictional coefficients to maximize clast movement.

Although the simulation approach we use in this analysis represents an advancement with respect to consideration of complex and heterogeneous clast shapes over a broad size range, it does not consider some factors that are likely to affect rubble deposits at the WIPP site. A notable omission is the large end of the clast size distribution. The simulations here have an upper limit of <~0.1 m, yet photographs of partially collapsed rooms show clasts with sizes on the order of meters (**Fig. 2**). These large clasts are likely to act as baffles for fluid-flow through rubble deposits given that they lack porosity. On the other hand, based on our simulation results, we can expect that many of them will be underlain by large "basal pocket" pores that could act as highly permeable, but localized, fluid-flow paths. In principle, simulations could be conducted that incorporate these large boulders and slabs in addition to the finer material considered in our analysis. Doing so, however, will require omitting the finest clast sizes, increasing

Lander, et al. Page 24 of 28

computational resources compared to those employed here, or improving the computational efficiency of the simulation code.

Our simulations represent the deposition process as a vertical "rain" of clasts. It is likely, however, that many clasts form in response to the fragmentation of large clasts on impact (3, 36). In such cases, there may be a significant lateral component to the clast trajectories during deposition, which might lead to somewhat different porosities compared to the depositional simulations in this study. Future work could consider this effect by explicitly simulating this fragmentation process. Alternatively, a similar lateral component in deposition could be obtained by dropping already simulated packs into larger containers, such that clasts will spread out laterally upon impact.

A final point for consideration is that the results presented here consider the initial state of the rubble deposits. Over time, this rubble will undergo decreases in porosity and permeability due to the creep closure of rooms that will occur in response to the stress conditions at the WIPP site and the weak material properties of salt (47). The rubble deposits will experience both lateral and vertical stresses, and consolidation will occur at the microscale in response to processes such as mechanical rearrangement, fracturing, crystal deformation, and pressure solution (e.g., 38).

5. SUMMARY AND CONCLUSIONS

Salt rubble deposits associated with the collapse of incompletely filled rooms in nuclear waste repositories are likely to have fluid transport and geomechanical properties that differ significantly from rooms with crushed salt backfill. Consequently, new models are needed to consider the potential influence of such rubble deposits on radionuclide release associated with borehole penetrations.

The methodology that we describe for simulating rubble porosity and 3D internal structure employs high-resolution depictions of clast shapes, and is capable of considering large variations in clast sizes. We demonstrate the application of this approach using clast shape and size data that we collected on run of mine material (ROM) from the WIPP located in southeastern New Mexico, USA. These clasts range in size from ~1–100 mm and have a mass averaged mean size of ~13 mm. From this effort, we obtained porosity values for simulated ROM rubble deposits that ranged from 34.1–38.6 vol% among six different, but stochastically equivalent simulations.

Simulations involving alternative input configurations reveal that porosity values are highly sensitive to clast size distributions, clast shapes, the extent of induced rearrangement, and frictional properties. In particular, porosity decreases by ~10 vol% with increasing polydispersity (standard deviation in phi of 0.18–1.5; equivalent to very well sorted–poorly sorted), and when spheres are substituted for shapes derived from micro-CT scans of WIPP ROM clasts. Simulated porosity values for rubble deposits also are highly sensitive to the frictional coefficient over a range of 0.01 to 1.0 (difference of ~11 vol%), but less so when considering a more reasonable range of uncertainty for salt clasts of 0.62 to 1.0 (difference of ~2 vol%). Similarly, although porosity may decline by as much as 10 vol% from extreme extents of rearrangement, a more realistic magnitude of 3% occurs for lower extents of induced rearrangement, consistent with laboratory experiments.

While the results we describe represent a step forward with respect to the goal of developing accurate models of salt rubble deposits, they omit several factors that are likely to be significant when considering the fluid transport properties of rubble at WIPP. The most important of these factors is that they do not consider the occurrence of meter-scale clasts. These large clasts are likely to have a complex effect on fluid flow through rubble deposits in that their lack of porosity will make them baffles for flow, yet large pores that are likely to occur below them could act as highly permeable, but localized, flow pathways.

Lander, et al. Page 25 of 28

STATEMENTS AND DECLARATIONS

Acknowledgements

Sandia National Laboratories is a multi-mission laboratory managed and operated by National Technology & Engineering Solutions of Sandia, LLC, a wholly owned subsidiary of Honeywell International Inc., for the U.S. Department of Energy's National Nuclear Security Administration under contract DE-NA0003525. This paper describes objective technical results and analysis. Any subjective views or opinions that might be expressed in the paper do not necessarily represent the views of the U.S. Department of Energy or the United States Government. This research is funded by WIPP programs administered by the Office of Environmental Management (EM) of the U.S. Department of Energy.

We thank Jon Matsukawa for his invaluable assistance in adapting Cyberclastic software for simulation of salt rubble deposition and Carl Jacques of Sandia National Laboratory's Nondestructive Environments and Diagnostics Department for conducting the micro-CT analyses.

Author Contributions

R. Lander: Conceptualization, Investigation, Methodology, Software, Visualization, Writing - original draft. **E. Matteo**: Conceptualization, Investigation, Writing - Review & Editing, Project administration. **L. Bonnell**: Conceptualization, Methodology, Writing - Review & Editing. **T. Dewers**: Conceptualization, Investigation. **M. Mills**: Investigation. **J. Guilkey**: Conceptualization, Writing - Review & Editing. **C. Mitchell**: Conceptualization, Writing - Review & Editing. **J. Stormont**: Investigation.

Conflicts of Interest

The authors declare that they have no conflicts of interest.

Data, Code & Protocol Availability

Data will be made available on request.

ORCID IDs

https://orcid.org/0009-0006-8046-8456 Robert Lander https://orcid.org/0000-0003-0585-2096 **Edward Matteo** https://orcid.org/0009-0004-8845-5153 Linda Bonnell https://orcid.org/0000-0003-2490-0751 Thomas Dewers https://orcid.org/0000-0002-1011-6977 Melisa Mills https://orcid.org/0000-0002-5375-0281 James Guilkey https://orcid.org/0000-0002-7376-5157 Chven Mitchell https://orcid.org/0000-0003-1238-8834 John Stormont

REFERENCES

- 1. Académie royale des sciences (France), & sciences (France), A. royale des. (C. Coulomb) (n.d.). *Mémoires de mathématique et de physique, presentés à l'Académie royale des sciences, par divers sçavans & lûs dans ses assemblées.* https://www.biodiversitylibrary.org/bibliography/4360
- 2. Al Ibrahim, M. A., Kerimov, A., Mukerji, T., & Mavko, G. (2019). Particula: A simulator tool for computational rock physics of granular media. *GEOPHYSICS*, 84(3), F85–F95. https://doi.org/10.1190/geo2018-0481.1
- 3. Babcock, E. (2022). Permeability and porosity of loose granular salt. *Civil Engineering ETDs*. https://digitalrepository.unm.edu/ce_etds/266
- 4. Bauer, S. J., Broome, S. T., Hansen, F. D., Lampe, B., Mills, M., & Stormont, J. (2015, June 28). Gas Flow Measurements of Consolidating Crushed Salt. 49th U.S. Rock Mechanics/Geomechanics Symposium, San Francisco, California. https://onepetro.org/ARMAUSRMS/proceedings-abstract/ARMA15/ARMA15/ARMA-2015-517/65889
- 5. Beard, D. C., & Weyl, P. K. (1973). Influence of texture on porosity and permeability of unconsolidated sand. AAPG Bulletin, 57. https://doi.org/10.1306/819A4272-16C5-11D7-8645000102C1865D
- 6. Börzsönyi, T., & Stannarius, R. (2013). Granular materials composed of shape-anisotropic grains. *Soft Matter*, 9(31), 7401–7418. https://doi.org/10.1039/C3SM50298H

Lander, et al. Page 26 of 28

7. Broome, S. T., Bauer, S. J., & Hansen, F. D. (2014). Reconsolidation of crushed salt to 250°c under hydrostatic and shear stress conditions. *AGU Fall Meeting Abstracts*, 2014, MR33A-2434. https://ui.adsabs.harvard.edu/abs/2012AGUFMMR33A2434B/abstract

- 8. Callahan, G. D., Loken, M. C., Hurtado, L. D., Hansen, F. D., & Sandia National Labs. (1996). Evaluation of constitutive models for crushed salt (No. SAND--96-0791C). Sandia National Labs., Albuquerque, NM (United States). https://inis.iaea.org/records/0gdrm-3vt61
- 9. Callahan, G. D., Mellegard, K. D., & Hansen, F. D. (1998). Constitutive behavior of reconsolidating crushed salt. *International Journal of Rock Mechanics and Mining Sciences*, 35(4–5), 422–423. https://doi.org/10.1016/S0148-9062(98)00045-X
- Camphouse, R. C., Gross, M., Herrick, C., & Thompson, B. (2012). Recommendations and Justifications of Parameter Values for the Run-of-Mine Salt Panel Closure System Design Modeled in the PCS-2012 PA. Memo to WIPP Records Center dated May 3, 2012. ERMS 557396. Carlsbad NM: Sandia National Laboratories. Appendix SCR: Feature, Event, and Process Screening for PA Subsection SCR-6.1.4.1.3, Screening Argument. https://wipp.energy.gov/library/CRA/CRA-2014/references/Others/Camphouse_Gross_Herrick_Kicker_Thompson_2012_ERMS557396m.pdf
- Case, J. B., Kelsall, P. C., & Withiam, J. L. (1987, June 29). Laboratory investigation of crushed salt consolidation. The 28th U.S. Symposium on Rock Mechanics (USRMS), Tucson, Arizona, USA. https://onepetro.org/ARMAUSRMS/proceedings-abstract/ARMA87/ARMA-87-0189/129837
- 12. Cho, G.-C., Dodds, J., & Santamarina, J. C. (2006). Particle shape effects on packing density, stiffness, and strength: Natural and crushed sands. *Journal of Geotechnical and Geoenvironmental Engineering*, 132(5), 591–602. https://doi.org/10.1061/(ASCE)1090-0241(2006)132:5(591)
- 13. Duran, J. (2000). Sands, Powders, and Grains. An Introduction to the Physics of Granular Materials. Springer. https://doi.org/10.1007/978-1-4612-0499-2
- Fagbemi, S., Tahmasebi, P., & Piri, M. (2018). Interaction between fluid and porous media with complex geometries: A direct pore-scale study. Water Resources Research, 54(9), 6336–6356. https://doi.org/10.1029/2017WR022242
- 15. Feret, L. R. (1930). La grosseur des grains des matières pulvérulentes. Premières Communications de La Nouvelle Association Internationale Pour l'Essai Des Matériaux, Groupe D, 428–436.
- 16. Folk, R. L. (1980). Petrology of sedimentary rocks. Hemphill Publishing Company. http://hdl.handle.net/2152/22930
- 17. Garcia, X., Akanji, L. T., Blunt, M. J., Matthai, S. K., & Latham, J. P. (2009). Numerical study of the effects of particle shape and polydispersity on permeability. *Physical Review E*, 80(2), 021304. https://doi.org/10.1103/PhysRevE.80.021304
- 18. Guilkey, J., Lander, R., & Bonnell, L. (2021). A hybrid penalty and grid based contact method for the Material Point Method. *Computer Methods in Applied Mechanics and Engineering*, 379, 113739. https://doi.org/10.1016/j.cma.2021.113739
- Guilkey, J., Lander, R., Bonnell, L., Matteo, E., & Mitchell, C. (2025). Numerical Simulations of Compaction of Salt Rubble for Use in Predictions of Fluid Transport Properties. In: Sobolik, S., Ingraham, M., Matteo, E., Mills, M., Ross, T., et al. (Eds). *The Mechanical Behavior of Salt XI*, CRC Press, Santa Fe, New Mexico, USA. https://doi.org/10.1201/9781003637349
- 20. Guo, Y., & Curtis, J. S. (2015). Discrete element method simulations for complex granular flows. *Annual Review of Fluid Mechanics*, 47(1), 21–46. https://doi.org/10.1146/annurev-fluid-010814-014644
- Hansen, F. D. (2014, June 1). Micromechanics of isochoric salt deformation. 48th U.S. Rock Mechanics/Geomechanics Symposium, Minneapolis, Minnesota, USA. https://onepetro.org/ARMAUSRMS/proceedings-abstract/ARMA14/ARMA14/ARMA-2014-7012/122327?redirectedFrom=PDF
- 22. Hansen, F. D., Bauer, S. J., Broome, S. T., & Callahan, G. D. (2012). Coupled Thermal-Hydrological-Mechanical Processes in Salt: Hot Granular Salt Consolidation, Constitutive Model and Micromechanics. In: FCRD-USED-2012-000422, U.S. Department of Energy, Office of Nuclear Energy, Office of Used Nuclear Fuel Disposition, Washington, D.C. SAND2012-9893P, Albuquerque, NM: Sandia National Laboratories. November 15, 2012.
- 23. Hansen, F., Popp, T., Wieczorek, K., & Stührenberg, D. (2015). Salt reconsolidation applied to repository seals. In: Roberts, L., Mellegard, K., Hansen, F. (Eds). *Mechanical Behaviour of Salt VIII*. CRC Press. 179-189. https://www.amazon.de/-/en/Mechanical-Behaviour-Salt-VIII-Proceedings/dp/1138028401
- 24. Haughey, D. P., & Beveridge, G. S. G. (1969). Structural properties of packed beds—A review. *The Canadian Journal of Chemical Engineering*, 47(2), 130–140. https://doi.org/10.1002/cjce.5450470206
- 25. Herman, A. (2022). Granular effects in sea ice rheology in the marginal ice zone. *Philosophical Transactions of the Royal Society A: Mathematical, Physical and Engineering Sciences*, 380(2235), 20210260. https://doi.org/10.1098/rsta.2021.0260

Lander, et al. Page 27 of 28

26. Holcomb, D. J., & Shields, M. (1987). Hydrostatic creep consolidation of crushed salt with added water. Sandia National Labs., Albuquerque, NM (USA).

- 27. Kerimov, A., Mavko, G., Mukerji, T., Dvorkin, J., & Al Ibrahim, M. A. (2018). The influence of convex particles' irregular shape and varying size on porosity, permeability, and elastic bulk modulus of granular porous media: Insights from numerical simulations. *Journal of Geophysical Research: Solid Earth*, 123(12). https://doi.org/10.1029/2018JB016031
- 28. Kröhn, K.-P., Zhang, C.-L., Czaikowski, O., & Heemann, D. S. & U. (2015). The compaction behaviour of salt backfill as a THM-process. In: Roberts, L., Mellegard, K., Hansen, F. (Eds). *Mechanical Behaviour of Salt VIII*. CRC Press. https://www.taylorfrancis.com/chapters/edit/10.1201/b18393-9/compaction-behaviour-salt-backfill-thm-process-kr%C3%B6hn-zhang-czaikowski-st%C3%BChrenberg-heemann?context=ubx&refId=7ca3fa81-b137-4e99-87dd-a57abfec57b4
- 29. Krumbein, W. C. (1934). Size frequency distributions of sediments. *SEPM Journal of Sedimentary Research*, Vol. 4. https://doi.org/10.1306/D4268EB9-2B26-11D7-8648000102C1865D
- 30. Lander, R., Guilkey, J., Bonnell, L., Matteo, E., & Mitchell, C. (2025, July 8). A step toward simulation of salt pressure solution in 3D granular packs. In: Sobolik, S., Ingraham, M., Matteo, E., Mills, M., Ross, T., et al. (Eds). *The Mechanical Behavior of Salt XI*, CRC Press, Santa Fe, New Mexico, USA. https://doi.org/10.1201/9781003637349
- 31. Lander, R. H., & Bonnell, L. M. (2020). Predicting sediment and sedimentary rock properties (United States Patent No. US10725012B2). https://patents.google.com/patent/US10725012B2/en
- 32. Lander, R. H., Cook, J. E., Guilkey, J., Kerimov, A., Bonnell, L. M., & Goodwin, L. B. (2024). Digital rock advances from a material point method approach for simulation of frame moduli and a sedimentary petrology-inspired method for creation of synthetic samples through simulation of deposition and diagenesis. *GEOPHYSICS*, 89(1), MR11–MR31. https://doi.org/10.1190/geo2023-0244.1
- 33. Liu, Y., Yu, Z., Yang, J., Wassgren, C., Curtis, J. S., & Guo, Y. (2020). Discrete element method investigation of binary granular flows with different particle shapes. *Energies*, 13(7), 1841. https://doi.org/10.3390/en13071841
- 34. Mair, K., Frye, K. M., & Marone, C. (2002). Influence of grain characteristics on the friction of granular shear zones. *Journal of Geophysical Research: Solid Earth*, 107(B10). https://doi.org/10.1029/2001JB000516
- 35. Mamao, K. Graphics and game gems database—Approximate convex decomposition for real-time collision detection. (n.d.). Retrieved July 9, 2025, from https://gameenginegems.com/gemsdb/article.php?id=504
- 36. Matteo, E. N., Mitchell, C. A. M., & Dewers, T. (2020). Characterization of permeability/porosity relationships as a function of rubble pile polydispersity during room closure at the waste isolation pilot plant. (Nos. SAND2020-2878C). Sandia National Lab. (SNL-NM), Albuquerque, NM (United States). https://www.osti.gov/biblio/1770056
- 37. Metcalf, J. R. (1966). Angle of repose and internal friction. *International Journal of Rock Mechanics and Mining Sciences & Geomechanics Abstracts*, 3(2), 155–161. https://doi.org/10.1016/0148-9062(66)90005-2
- 38. Mills, M. M., Stormont, J. C., & Bauer, S. J. (2018). Micromechanical processes in consolidated granular salt. *Engineering Geology*, 239, 206–213. https://doi.org/10.1016/j.enggeo.2018.03.024
- 39. Montgomery, D. C., & Runger, G. C. (2019). Applied Statistics and Probability for Engineers, EMEA Edition (7th ed.). Wiley & Sons Ltd. https://www.wiley-vch.de/de/fachgebiete/ingenieurwesen/applied-statistics-and-probability-for-engineers-emea-edition-978-1-119-58559-6
- 40. Nguyen, D.-H., Azéma, E., Radjai, F., & Sornay, P. (2014). Effect of size polydispersity versus particle shape in dense granular media. *Physical Review E*, 90(1), 012202. https://doi.org/10.1103/PhysRevE.90.012202
- 41. NVIDIA Corporation. (n.d.). NVIDIA Developer / Physx sdk. https://developer.nvidia.com/physx-sdk
- 42. NVIDIA Corporation (2021). NVIDIA PhysX SDK 4.1 (Nvidiagameworks/physx. [C++]. NVIDIA GameWorks). https://github.com/NVIDIAGameWorks/PhysX
- 43. Oquendo-Patiño, W. F., & Estrada, N. (2022). Finding the grain size distribution that produces the densest arrangement in frictional sphere packings: Revisiting and rediscovering the century-old Fuller and Thompson distribution. *Physical Review E*, 105(6), 064901. https://doi.org/10.1103/PhysRevE.105.064901
- 44. Parker, A. R., Lander, R. H., Bonnell, L. M., Gianniny, G. L. (2016). A fresh look at controls on sand depositional porosity. Rocky Mountain Section 68th Annual Meeting 2016. https://gsa.confex.com/gsa/2016RM/webprogram/Paper275871.html
- 45. Pettijohn, F. J., Potter, P. E., & Siever, R. (1973). Sand and Sandstone. Springer US. https://doi.org/10.1007/978-1-4615-9974-6
- 46. Powers, D. W., Lambert, S. J., Shaffer, S. E., & Hill, L. R. (1978). Geological characterization report, waste isolation pilot plant (Wipp) site, southeastern New Mexico (W. D. Weart, Ed.; No. SAND-78-1596(Vol.1), 6441454; p. SAND-78-1596(Vol.1), 6441454). https://doi.org/10.2172/6441454
- 47. Reedlunn, B., Moutsanidis, G., Baek, J., Huang, T.-H., Koester, J., et al. (2019). Initial simulations of empty room collapse and reconsolidation at the waste isolation pilot plant (No. SAND--2019-15351, 1592852, 681972); p. SAND--2019-15351, 1592852, 681972). https://doi.org/10.2172/1592852

Lander, et al. Page 28 of 28

48. Sanchidrián, J. A., Ouchterlony, F., Segarra, P., & Moser, P. (2014). Size distribution functions for rock fragments. *International Journal of Rock Mechanics and Mining Sciences*, 71, 381–394. https://doi.org/10.1016/j.ijrmms.2014.08.007

- 49. Spiers, C. J., & Brzesowsky, R. H. (1993). Densification Behavior of Wet Granular Salt: Theory versus Experiment. *Seventh Symposium on Salt , Vol. 1*, 83–92. https://www.amazon.com/Seventh-Symposium-Salt-Hidetake-Kakihana/dp/0444891439
- 50. Spiers, C. J., & Carter, N. (1998). Microphysics of Rocksalt flow in nature. In: Aubertin, M., Hardy Jr.H.R. (Eds.). *The Mechanical Behaviour of Salt: Vol. IV. Trans. Tech.* https://www.google.com/books/edition/Mechanical_Behavior_of_Salt/saJTwgEACAAJ?hl=en&kptab=overview
- 51. Spiers, C. J., Schutjens, P. M., Brzesowsky, R. H., Peach, C. J., Liezenberg, J. L., & Zwart, H. J. (1990). Experimental determination of constitutive parameters governing creep of rocksalt by pressure solution. Geological Society, London, Special Publications, 54, 215–227. https://doi.org/https://doi.org/10.1144/GSL.SP.1990.054.01.21
- 52. Stein, C. L. (1985). Mineralogy in the waste isolation pilot plant (Wipp) facility stratigraphic horizon (No. SAND-85-0321, 5203761; p. SAND-85-0321, 5203761). https://doi.org/10.2172/5203761
- 53. Stokes, G. G. (1851). On the Effect of the Internal Friction of Fluids on the Motion of Pendulums. In: *Transactions of the Cambridge Philosophical Society*, Vol. IX, pg. 8–106. https://mural.uv.es/daroig/documentos/stokes1850.pdf.
- 54. Stone, C. M. (1997). Final disposal room structural response calculations (No. SAND--97-0795, 510306; p. SAND--97-0795, 510306). https://doi.org/10.2172/510306
- 55. Stormont, J. C. (1990). Discontinuous behavior near excavations in a bedded salt formation (No. SAND-89-2403, 6461949; p. SAND-89-2403, 6461949). https://doi.org/10.2172/6461949
- Stührenberg, D. (2007). Long-term Laboratory Investigation on Backfill. In M. Wallner, K.-H. Lux, W. Minkley, & H. R. Hardy (Eds.), *The Mechanical Behavior of Salt Understanding of THMC Processes in Salt* (1st ed.). CRC Press. https://doi.org/10.1201/9781315106502
- 57. Stührenberg, D., & Schulze, O. (2012). Porosity and permeability of crushed and damaged rock salt during compaction. In: P. Bérest, M. Ghoreychi, F. Hadj-Hassen, & M. Tijani (Eds.). *Mechanical Behaviour of Salt VII*. CRC Press. https://doi.org/10.1201/b12041
- 58. Sweijen, T., Hassanizadeh, S. M., Aslannejad, H., & Leszczynski, S. (2020). The effect of particle shape on porosity of swelling granular materials: Discrete element method and the multi-sphere approximation. *Powder Technology*, 360, 1295–1304. https://doi.org/10.1016/j.powtec.2019.09.036
- 59. Takai, H. (2013). Report 10: Simulation of salt particle trajectory from spreader disc to road surface: Basic consideration and equations. Aarhus University, Engineering Centre Bygholm, Test and Development. https://pure.au.dk/ws/files/68256757/Report_10_Simulation_method.pdf
- 60. Taylor, T. R., Lander, R. H., & Bonnell, L. M. (2022). Sandstone petrography, petrology, and modeling. *SEPM Society for Sedimentary Geology*. https://doi.org/10.2110/sepmcsp.13
- 61. Tolomeo, M., & McDowell, G. R. (2022). Modelling real particle shape in DEM: A comparison of two methods with application to railway ballast. *International Journal of Rock Mechanics and Mining Sciences*, 159, 105221. https://doi.org/10.1016/j.ijrmms.2022.105221
- 62. Tonge, R., Benevolenski, F., & Voroshilov, A. (2012). Mass splitting for jitter-free parallel rigid body simulation. *ACM Transactions on Graphics*, 31(4), 1–8. https://doi.org/10.1145/2185520.2185601
- 63. Tounsi, H., Lerche, S., Wolters, R., Hu, M., & Rutqvist, J. (2023). Impact of the compaction behavior of crushed salt on the thermo-hydro-mechanical response of a generic salt repository for heat-generating nuclear waste. *Engineering Geology*, 323, 107217. https://doi.org/10.1016/j.enggeo.2023.107217
- 64. Trask, P. D. (1930). Mechanical analyses of sediments by centrifuge. *Economic Geology*, 25(6), 581–599. https://doi.org/10.2113/gsecongeo.25.6.581
- 65. US DOE (2014). Title 40 CFR part 191 subparts B and C compliance recertification application for the Waste Isolation Pilot Plant, Carlsbad, NM. Tech. rep. DOE/WIPP 2014-3503. US Department of Energy: Carlsbad Field Office. https://wipp.energy.gov/library/CRA/CRA%202019/US%20DOE/USDOE%20%202014%20%20DOE-WIPP%2014-3503.pdf
- 66. US DOE (2015). Accident investigation report phase 2. Radiological release event at the Waste Isolation Pilot Plant on February 14, 2014. Tech. rep. United States Department of Energy Office of Environmental Management. https://www.energy.gov/sites/prod/files/2016/06/f33/WIPP-Radiological-Release-Event-Phase-2-04-16-2015.pdf
- 67. Xu, W., Zhang, K., Zhang, Y., & Jiang, J. (2022). Packing fraction, tortuosity, and permeability of granular-porous media with densely packed spheroidal particles: Monodisperse and polydisperse systems. *Water Resources Research*, 58(2), e2021WR031433. https://doi.org/10.1029/2021WR031433
- 68. Zhao, S., & Zhao, J. (2021). SudoDEM: Unleashing the predictive power of the discrete element method on simulation for non-spherical granular particles. *Computer Physics Communications*, 259, 107670. https://doi.org/10.1016/j.cpc.2020.107670